Title
An adaptive space-time phase field formulation for dynamic fracture of brittle shells based on LR NURBS

Journal
Computational Mechanics, 65(4)

ISSN
0178-7675

Authors
Paul, Karsten
Zimmermann, Christopher
Mandadapu, Kranthi K
et al.

Publication Date
2020-04-01

DOI
10.1007/s00466-019-01807-y

Peer reviewed

An adaptive space-time phase field formulation for dynamic fracture of brittle shells based on LR NURBS

Karsten Paul*, Christopher Zimmermann*, Kranthi K. Mandadapu†§, Thomas J.R. Hughes‡, Chad M. Landis‡, Roger A. Sauer*[1]

*Aachen Institute for Advanced Study in Computational Engineering Science (AICES), RWTH Aachen University, Templergraben 55, 52062 Aachen, Germany

†Department of Chemical and Biomolecular Engineering, University of California at Berkeley, 110A Gilman Hall, Berkeley, CA 94720-1460, USA

§Chemical Sciences Division, Lawrence Berkeley National Laboratory, CA 94720, USA

‡The Oden Institute for Computational Engineering and Sciences, The University of Texas at Austin, 201 E. 24th Street, POB 4.102, 1 University Station (C0200), Austin, TX 78712-1229, USA

Abstract

We present an adaptive space-time phase field formulation for dynamic fracture of brittle shells. Their deformation is characterized by the Kirchhoff-Love thin shell theory using a curvilinear surface description. All kinematical objects are defined on the shell's mid-plane. The evolution equation for the phase field is determined by the minimization of an energy functional based on Griffith's theory of brittle fracture. Membrane and bending contributions to the fracture process are modeled separately and a thickness integration is established for the latter. The coupled system consists of two nonlinear fourth-order PDEs and all quantities are defined on an evolving two-dimensional manifold. Since the weak form requires C^1-continuity, isogeometric shape functions are used. The mesh is adaptively refined based on the phase field using Locally Refinable (LR) NURBS. Time is discretized based on a generalized-α method using adaptive time-stepping, and the discretized coupled system is solved with a monolithic Newton-Raphson scheme. The interaction between surface deformation and crack evolution is demonstrated by several numerical examples showing dynamic crack propagation and branching.

Keywords: Phase fields, brittle fracture, isogeometric analysis, adaptive local refinement, LR NURBS, nonlinear finite elements, Kirchhoff-Love shells

1 Introduction

The need for shortening development cycles of engineering components requires efficient computational methods. The robustness requirements for these components are increasing so that the prediction of structural defects and failure plays a major role in current development processes. It is therefore important to have efficient and reliable computational methods for predicting fracture. Several computational methods have been introduced to model crack growth. The most important ones in the framework of finite elements are described subsequently.

Sharp interface models introduce discontinuities within the body in order to model cracks. In the *extended finite element method* by Moës et al. (1999), the basis functions are enriched by

[1]corresponding author, email: sauer@aices.rwth-aachen.de

discontinuities to model the displacement jump across cracks. In contrast to this, a crack can be introduced by a modification of the finite element mesh as in the *virtual crack closure technique* (Krueger, 2002). Similar to the *extended finite element method*, Remmers et al. (2003) also enrich the basis in the *cohesive segments method*. Since the location of the crack has to be known, it has to be numerically tracked, which tends to be a tedious task, especially in three dimensions.

Thus, *diffuse interface models* have gained popularity for modeling brittle fracture. In the *phase field method* no discontinuities are introduced within the body. Instead, the crack is smoothed out and described by a small transition zone that ranges between undamaged and fully fractured material. Phase field methods describe the evolving cracks by an additional partial differential equation (PDE) such that there is no need for tracking the interface. For complex crack patterns including nucleation, branching, and merging, phase field formulations have been shown to be very effective.

Based on the thermodynamic considerations of brittle fracture by Griffith (1921), a variational formulation of brittle fracture has been introduced by Francfort and Marigo (1998). Their formulation includes the minimization of a global energy functional to model the quasi-static fracture process. A corresponding phase field implementation within the finite element method has been presented by Bourdin et al. (2000). The robustness and accuracy of the variational formulation in two and three dimensions using phase field methods have been demonstrated by e.g. Miehe et al. (2010a) and Miehe et al. (2010b). Successful extensions to dynamic problems have been presented by Larsen (2010), Larsen et al. (2010), Bourdin et al. (2011), Borden et al. (2012), Hofacker and Miehe (2012) and Schlüter et al. (2014). In contrast to the variational formulation of brittle fracture, Karma et al. (2001) and Kuhn and Müller (2010) use a phase transition framework based on the Ginzburg-Landau equation. The latter is more often used in the physics community, where a very general phase field formulation is applied to fracture mechanics. A stabilization for quasi-static simulations using a monolithic solution approach for the coupled system is proposed by Gerasimov and De Lorenzis (2016). Gerasimov et al. (2018) apply a non-intrusive global/local approach in a phase field framework for brittle fracture, in which at first the structural analysis of the whole domain is performed and, afterwards, local regions where fracture is predicted are re-analyzed. These steps are then repeated until convergence is obtained. Ambati et al. (2015) summarize several phase field formulations for brittle fracture. In the work of Kuhn et al. (2015) the influence of different degradation functions on the solution has been investigated. Similar investigations have been made by Sargado et al. (2018) who have also studied parametric degradation functions. Possibilities to enforce irreversibility of the fracture process are presented in detail in the work of Gerasimov and De Lorenzis (2018), especially focusing on the penalty method. The authors also derive a lower bound for the penalty parameter for a quasi-static second-order phase field model for brittle fracture.

The majority of the published phase field methods for fracture use a second-order phase field formulation. The high order differential operators of the phase field PDE stemming from the crack density functional of Borden et al. (2014), which is used in this work, and the equation of motion of the shell framework require a spatial finite element discretization that is at least C^1-continuous. Isogeometric Analysis (IGA), proposed by Hughes et al. (2005), allows for user-defined smoothness of the solution within the finite element framework. Within IGA, the smoothness is most commonly achieved through the use of B-Spline- and NURBS-based shape functions. Since phase field methods require a highly resolved finite element mesh in the transition zone, local refinement methods are commonly used in the context of phase field methods for fracture. The introduction of hierarchical B-splines by Forsey and Bartels (1988) has offered the possibility of local refinement within an IGA framework. The extension to the local refinement of NURBS is for instance given by Sederberg et al. (2003) by introducing T-

Splines. Another approach that allows local refinement is Locally Refinable (LR) splines. LR B-splines were first introduced by Dokken et al. (2013) and further advanced by Johannessen et al. (2014). Their extension to LR NURBS is provided by Zimmermann and Sauer (2017). Isogeometric collocation methods (Gomez et al., 2014; Reali and Hughes, 2015) for phase field models of fracture are also introduced, for instance by Schillinger et al. (2015).

Hesch et al. (2016b) employ a hierarchical refinement scheme within a higher order phase field model. Similarly, Hesch et al. (2016a) couple a model for frictional contact to a higher order phase field model using hierarchical NURBS. Kästner et al. (2016) investigate phase field models by comparing adaptive refinement based on locally refined hierarchical B-splines with uniformly refined discretizations. Borden et al. (2012) propose an adaptive refinement strategy using T-splines and use the phase field value itself to identify the need for local refinement. Mesh adaptivity schemes, in which a predictor-corrector scheme is used, are employed by Zhou and Zhuang (2018) for modeling fracture in rocks and by Badnava et al. (2018) to model mechanically and thermo-mechanically induced cracks. In these approaches, the system is solved and then checked for the need of mesh refinement. In the work by Nagaraja et al. (2018) a multi-level hp-refinement technique has been established using the finite cell method (Parvizian et al., 2007) to model brittle fracture in two dimensions.

Many papers concerning the computational modeling of shells within an isogeometric framework have been published, for instance by Benson et al. (2013), Echter et al. (2013), Kiendl et al. (2015) and Duong et al. (2017). Since for shells the bending stress varies across the thickness, a suitable split of the energy within the fracture model has to be established. In the work by Ulmer et al. (2012) brittle fracture in thin plates and shells is modeled. They combine a plate and a standard membrane to model the shell but have only split the membrane and not the bending part of the elastic energy. Thus, the whole bending energy contributes to crack evolution and is degraded in regions of damage. Amiri et al. (2014) do not employ an energy split, which limits their model to shells under pure tension. In the work by Ambati and De Lorenzis (2016) the shell and the phase field are also discretized over the thickness. Areias et al. (2016) utilize two phase fields, one for the top and the other one for the bottom face of the shell. This framework is also used by Reinoso et al. (2017) for a 6-parameter shell model. Their formulation results in a non-constant phase field throughout the thickness. In contrast to this, Kiendl et al. (2016) use a constant phase field over the thickness but use thickness integration to split the whole energy into a tensile part, which contributes to crack growth, and a compressive part, which does not.

Zimmermann et al. (2019) model Cahn-Hillard phase field equations on deforming surfaces based on the shell formulation of Duong et al. (2017). Even though a different physical process is modeled, the resulting coupled finite element formulation is similar to the one proposed here.

In this paper we establish a dynamic brittle fracture framework within the nonlinear IGA thin shell formulation of Duong et al. (2017), in which shells with arbitrarily large curvature or doubly curved shells can be modeled. Its hyperelastic material model allows for large deformations and is given as a sum of membrane and bending contributions. The proposed higher order phase field model of Borden et al. (2014) is adopted because of its higher rate of convergence and it is formulated on the shell's mid-plane. Motivated by the work of Kiendl et al. (2016), bending effects on the fracture process are modeled based on thickness integration. Adaptive spatial refinement is based on LR NURBS (Zimmermann and Sauer, 2017) and temporal discretization is based on the generalized-α scheme (Chung and Hulbert, 1993). The time steps are adjusted based on the number of Newton-Raphson iterations required during the last time step. In summary, the proposed formulation contains the following features:

- It couples a higher-order phase field model for fracture with a nonlinear shell formulation.

- It is formulated in curvilinear coordinates, and applicable to general shell configurations.
- The coupled system is solved within a monolithic, fully implicit solution approach.
- It uses adaptive local refinement in space and time.
- The spatial discretization is based on LR NURBS.
- An energy split is used in which the membrane and bending energies are split separately.

The subsequent sections are structured as follows: Sec. 2 summarizes the surface description and kinematics. The balance laws and the equation of motion are derived in Sec. 3. Sec. 4 introduces the energy minimization problem and the material model employed. Extensions to degradation, irreversibility and an energy split are also presented. Based on the Euler-Lagrange equation, the Helmholtz free energy is minimized, which leads to the governing equation for the phase field's evolution. The discretization of the coupled problem is described in Sec. 5. Numerical examples are presented in Sec. 6 to illustrate crack propagation on curved surfaces. Conclusions are drawn in Sec. 7.

2 Deforming surfaces

This section summarizes the thin shell formulation in the framework of curvilinear coordinates and Kichhoff-Love kinematics. A more detailed presentation can be found in Sauer (2018).

2.1 Surface description

A curved surface $\mathcal{S}$ in 3D space can be characterized by the parametric description at any time t by the function

$$\boldsymbol{x} = \boldsymbol{x}(\xi^\alpha, t)\,, \quad \alpha = 1, 2\,, \tag{1}$$

where ξ^α denote the curvilinear coordinates associated with a material point $\boldsymbol{x} \in \mathcal{S}$. ξ^α are convected along with the material deformation of the surface and hence, they are also called *convected coordinates*. The co-variant tangent vectors at $\boldsymbol{x}$ are given by

$$\boldsymbol{a}_\alpha := \frac{\partial \boldsymbol{x}}{\partial \xi^\alpha}\,. \tag{2}$$

From these follow the surface metric

$$a_{\alpha\beta} := \boldsymbol{a}_\alpha \cdot \boldsymbol{a}_\beta\,, \tag{3}$$

the surface normal

$$\boldsymbol{n} := \frac{\boldsymbol{a}_1 \times \boldsymbol{a}_2}{\|\boldsymbol{a}_1 \times \boldsymbol{a}_2\|}\,, \tag{4}$$

and the contra-variant tangent vectors

$$\boldsymbol{a}^\alpha = a^{\alpha\beta}\,\boldsymbol{a}_\beta\,, \tag{5}$$

where $[a^{\alpha\beta}] = [a_{\alpha\beta}]^{-1}$. All Greek indices range from 1 to 2 and are summed when repeated. Based on the second parametric derivative $\boldsymbol{a}_{\alpha,\beta} := \partial \boldsymbol{a}_\alpha / \partial \xi^\beta$, the curvature tensor components

$$b_{\alpha\beta} = \boldsymbol{a}_{\alpha,\beta} \cdot \boldsymbol{n}\,, \tag{6}$$

follow. The set of initial surface points $\boldsymbol{X} \in \mathcal{S}_0$ follows from $\boldsymbol{X} := \boldsymbol{x}(\xi^\alpha, 0)$. In analogy to Eqs. (2)–(6), we define the surface quantities $\boldsymbol{A}_\alpha := \partial \boldsymbol{X}/\partial \xi^\alpha$, $A_{\alpha\beta} := \boldsymbol{A}_\alpha \cdot \boldsymbol{A}_\beta$, $\boldsymbol{N} := \boldsymbol{A}_1 \times \boldsymbol{A}_2 / \|\boldsymbol{A}_1 \times \boldsymbol{A}_2\|$, $\boldsymbol{A}^\alpha := A^{\alpha\beta}\boldsymbol{A}_\beta$, $[A^{\alpha\beta}] := [A_{\alpha\beta}]^{-1}$ and $B_{\alpha\beta} := \boldsymbol{A}_{\alpha,\beta} \cdot \boldsymbol{N}$ at $t = 0$ as a reference configuration, denoted $\mathcal{S}_0$. The surface gradient

$$\mathrm{grad}_\mathrm{S}\phi \;=\; \nabla_\mathrm{S}\phi \;:=\; \phi_{;\alpha}\, \boldsymbol{A}^\alpha, \tag{7}$$

and surface Laplacian

$$\Delta_\mathrm{S}\phi \;:=\; \nabla_\mathrm{S} \cdot \nabla_\mathrm{S}\phi \;=\; \phi_{;\alpha\beta}\, A^{\alpha\beta}\,, \tag{8}$$

can be defined based on the parametrization in Eq. (1). Here, ϕ denotes a general scalar function and the subscript ';' indicates the co-variant derivative. It is equal to the parametric derivative for general scalars, i.e. $\phi_{;\alpha} = \phi_{,\alpha} := \partial\phi/\partial\xi^\alpha$. But, $\phi_{;\alpha\beta} \neq \phi_{,\alpha\beta}$ and instead

$$\phi_{;\alpha\beta} \;=\; \phi_{,\alpha\beta} - \hat{\Gamma}^\gamma_{\alpha\beta}\, \phi_{,\gamma}\,, \tag{9}$$

where $\hat{\Gamma}^\gamma_{\alpha\beta} = \boldsymbol{A}_{\alpha,\beta} \cdot \boldsymbol{A}^\gamma$ are the Christoffel symbols of the second kind on surface $\mathcal{S}_0$. On $\mathcal{S}$, these read $\Gamma^\gamma_{\alpha\beta} = \boldsymbol{a}_{\alpha,\beta} \cdot \boldsymbol{a}^\gamma$.

2.2 Surface kinematics

The relation between reference surface $\mathcal{S}_0$ and current surface $\mathcal{S}$ is described by the surface deformation gradient

$$\boldsymbol{F} = \boldsymbol{a}_\alpha \otimes \boldsymbol{A}^\alpha\,. \tag{10}$$

The left surface Cauchy-Green tensor then follows as

$$\boldsymbol{B} = A^{\alpha\beta}\, \boldsymbol{a}_\alpha \otimes \boldsymbol{a}_\beta\,, \tag{11}$$

with its two invariants

$$I_1 := A^{\alpha\beta}\, a_{\alpha\beta} \quad \text{and} \quad J := \sqrt{\det[A^{\alpha\beta}]\det[a_{\alpha\beta}]}\,. \tag{12}$$

The latter characterizes the surface stretch between $\mathcal{S}_0$ and $\mathcal{S}$. The surface Green-Lagrange strain tensor and the symmetric relative curvature tensor are

$$\begin{aligned} \boldsymbol{E} \;&=\; \frac{1}{2}\,(a_{\alpha\beta} - A_{\alpha\beta})\, \boldsymbol{A}^\alpha \otimes \boldsymbol{A}^\beta, \\ \boldsymbol{K} \;&=\; (b_{\alpha\beta} - B_{\alpha\beta})\, \boldsymbol{A}^\alpha \otimes \boldsymbol{A}^\beta. \end{aligned} \tag{13}$$

The material time derivative is denoted by

$$\dot{(...)} := \left.\frac{\partial ...}{\partial t}\right|_{\xi^\alpha = \text{fixed}}. \tag{14}$$

This leads to the material velocity at $\boldsymbol{x}$

$$\boldsymbol{v} := \dot{\boldsymbol{x}}\,, \tag{15}$$

and the rates

$$\dot{\boldsymbol{a}}_\alpha = \boldsymbol{v}_{,\alpha} = \frac{\partial \boldsymbol{v}}{\partial \xi^\alpha}\,, \quad \text{and} \quad \dot{a}_{\alpha\beta} = \boldsymbol{a}_\alpha \cdot \dot{\boldsymbol{a}}_\beta + \dot{\boldsymbol{a}}_\alpha \cdot \boldsymbol{a}_\beta\,. \tag{16}$$

2.3 Surface variations

The variation of various surface measures is required for the formulation of the weak form of the thin shell equation. Particularly important are the variations

$$\begin{aligned} \delta a_{\alpha\beta} &= \boldsymbol{a}_\alpha \cdot \delta\boldsymbol{a}_\beta + \delta\boldsymbol{a}_\alpha \cdot \boldsymbol{a}_\beta \,, \\ \delta b_{\alpha\beta} &= \left(\delta\boldsymbol{a}_{\alpha,\beta} - \Gamma^\gamma_{\alpha\beta}\, \delta\boldsymbol{a}_\gamma\right) \cdot \boldsymbol{n} \,, \\ \delta\boldsymbol{n} &= -(\boldsymbol{a}^\alpha \otimes \boldsymbol{n})\, \delta\boldsymbol{a}_\alpha \,, \end{aligned} \tag{17}$$

where $\delta\boldsymbol{a}_\alpha = \delta\boldsymbol{x}_{,\alpha}$ and $\delta\boldsymbol{a}_{\alpha,\beta} = \delta\boldsymbol{x}_{,\alpha\beta}$. Here, $\delta\boldsymbol{x}$ denotes a kinematically admissible variation of the deformation. Additional variations of surface quantities are provided in Sauer and Duong (2017).

3 Thin shell theory

The governing equations for the shell are summarized in the following. Equilibrium is given in strong and weak form. Considering Kirchhoff-Love kinematics, the constitutive behavior of thin shells can be fully characterized by the quantities $a_{\alpha\beta}$ and $b_{\alpha\beta}$.

3.1 Balance of linear and angular momentum

The equation of motion

$$\rho\, \dot{\boldsymbol{v}} = \boldsymbol{T}^\alpha_{;\alpha} + \boldsymbol{f} \,, \quad \forall\, \boldsymbol{x} \in \mathcal{S} \,, \tag{18}$$

follows from the balance of linear momentum for surface $\mathcal{S}$. $\boldsymbol{f} = f^\alpha\, \boldsymbol{a}_\alpha + p\, \boldsymbol{n}$ denotes prescribed body forces and

$$\boldsymbol{T}^\alpha = N^{\alpha\beta}\, \boldsymbol{a}_\beta + S^\alpha\, \boldsymbol{n} \,, \tag{19}$$

are the stress vectors that include the in-plane membrane components $N^{\alpha\beta}$ and the out-of-plane shear components S^α (Naghdi, 1973; Steigmann, 1999; Sauer and Duong, 2017). These are related to the stress tensor

$$\boldsymbol{\sigma} = N^{\alpha\beta} \boldsymbol{a}_\alpha \otimes \boldsymbol{a}_\beta + S^\alpha \boldsymbol{a}_\alpha \otimes \boldsymbol{n} \,, \tag{20}$$

through Cauchy's formula $\boldsymbol{T}^\alpha = \boldsymbol{\sigma}^{\mathrm{T}} \boldsymbol{a}^\alpha$. Given the outward pointing normal $\boldsymbol{\nu} = \nu_\alpha \boldsymbol{a}^\alpha$ at a cut through $\mathcal{S}$, the traction $\boldsymbol{T} = \boldsymbol{\sigma}^{\mathrm{T}} \boldsymbol{\nu} = \boldsymbol{T}^\alpha \nu_\alpha$ acting on this cut follows.
Likewise, the moment vector on the cut reads $\boldsymbol{M} = \boldsymbol{\mu}^{\mathrm{T}} \boldsymbol{\nu}$ with the moment tensor

$$\boldsymbol{\mu} = -M^{\alpha\beta} \boldsymbol{a}_\alpha \otimes \boldsymbol{a}_\beta \,, \tag{21}$$

where $M^{\alpha\beta}$ denotes its in-plane components (Sauer and Duong, 2017; Sahu et al., 2017). The balance of angular momentum yields

$$\begin{aligned} S^\alpha &= -M^{\beta\alpha}_{;\beta} \,, \\ \sigma^{\alpha\beta} &= \sigma^{\beta\alpha} \,, \end{aligned} \tag{22}$$

where $\sigma^{\alpha\beta} := N^{\alpha\beta} - b^\beta_\gamma M^{\gamma\alpha}$. The stress components $\sigma^{\alpha\beta}$ and $M^{\alpha\beta}$ follow from constitution, which is discussed in Sec. 4.2.
The component form of the equation of motion

$$\begin{aligned} \rho\, a^\alpha &= f^\alpha + N^{\lambda\alpha}_{;\lambda} - S^\lambda b^\alpha_\lambda \,, \\ \rho\, a_{\mathrm{n}} &= p + N^{\alpha\beta} b_{\alpha\beta} + S^\alpha_{;\alpha} \,, \end{aligned} \tag{23}$$

is obtained by combining Eqs. (18), (20) and (22.1). Here, $a^\alpha := \dot{\boldsymbol{v}} \cdot \boldsymbol{a}^\alpha$, $a_{\mathrm{n}} := \dot{\boldsymbol{v}} \cdot \boldsymbol{n}$, $f^\alpha := \boldsymbol{f} \cdot \boldsymbol{a}^\alpha$ and $p := \boldsymbol{f} \cdot \boldsymbol{n}$.

3.2 Weak form for deforming thin shells

The weak form for Kirchhoff-Love shells is given by (Sauer and Duong, 2017; Sauer et al., 2017)

$$G_{\text{kin}} + G_{\text{int}} - G_{\text{ext}} = 0\,, \quad \forall\, \delta\boldsymbol{x} \in \mathcal{U}\,, \tag{24}$$

with

$$\begin{aligned} G_{\text{kin}} &:= \int_{\mathcal{S}} \delta\boldsymbol{x} \cdot \rho\, \dot{\boldsymbol{v}}\, \mathrm{d}a\,, \\ G_{\text{int}} &:= \int_{\mathcal{S}} \frac{1}{2}\, \delta a_{\alpha\beta}\, \sigma^{\alpha\beta}\, \mathrm{d}a + \int_{\mathcal{S}} \delta b_{\alpha\beta}\, M^{\alpha\beta}\, \mathrm{d}a\,, \\ G_{\text{ext}} &:= \int_{\mathcal{S}} \delta\boldsymbol{x} \cdot \boldsymbol{f}\, \mathrm{d}a + \int_{\partial_t\mathcal{S}} \delta\boldsymbol{x} \cdot \boldsymbol{T}\, \mathrm{d}s + \int_{\partial_m\mathcal{S}} \delta\boldsymbol{n} \cdot \boldsymbol{M}\, \mathrm{d}s\,. \end{aligned} \tag{25}$$

Here,

$$\mathcal{U} = \left\{ \delta\boldsymbol{x} \in \tilde{\mathcal{H}}^2\big(\mathcal{S}(\boldsymbol{x},t)^3\big) \,|\, \delta\boldsymbol{x} = 0 \,\text{on}\, \partial_x\mathcal{S}\,,\ \delta\boldsymbol{n} = 0 \,\text{on}\, \partial_n\mathcal{S} \right\}\,, \tag{26}$$

is the space of suitable surface variations, where $\tilde{\mathcal{H}}^2$ is the Sobolev space of Lebesgue square integrable functions and $\partial_x\mathcal{S}$ and $\partial_n\mathcal{S}$ are the Dirichlet boundaries for displacements and rotations. The prescribed edge tractions $\boldsymbol{T} = \boldsymbol{\sigma}^{\mathrm{T}}\boldsymbol{\nu}$ and edge moments $\boldsymbol{M} = \boldsymbol{\mu}^{\mathrm{T}}\boldsymbol{\nu}$ act on the boundaries $\partial_t\mathcal{S}$ and $\partial_m\mathcal{S}$ with the outward normal $\boldsymbol{\nu} = \nu_\alpha \boldsymbol{a}^\alpha$. We note that the torsional components of the moment $\boldsymbol{M}$ are perceived as an effective shear traction in Kirchhoff-Love shells, e.g. see Sauer and Duong (2017). If desired, $\mathrm{d}a = J\,\mathrm{d}A$ and $\rho\,\mathrm{d}a = \rho_0\,\mathrm{d}A$ can be used to map integrals to the reference surface $\mathcal{S}_0$. The components $\sigma^{\alpha\beta}$ and $M^{\alpha\beta}$ follow from the constitutive laws as outlined in Sec. 4.2.

4 Fracture of deforming surfaces

The formulation for the modeling of brittle fracture is based on Griffith's theory (Griffith, 1921), in which the energy release rate E_{G} of a body, which describes the dissipated energy during crack evolution, is related to the fracture toughness $\mathcal{G}_{\text{c}}\,[\text{J}\,\text{m}^{-2}]$. The latter is also referred to as the critical fracture energy density or critical energy release rate. The corresponding Kuhn-Tucker conditions read

$$E_{\text{G}} - \mathcal{G}_{\text{c}} \leq 0, \qquad \dot{c} \geq 0, \qquad (E_{\text{G}} - \mathcal{G}_{\text{c}})\,\dot{c} = 0\,, \tag{27}$$

with $\dot{c}$ denoting the crack propagation velocity. Since crack nucleation and branching are not captured by this formulation, Griffith's theory has been reformulated as a global energy minimization problem (Francfort and Marigo, 1998). The corresponding energy functional is derived subsequently.

4.1 Helmholtz free energy

The total energy in the system is given by

$$\Pi := \Pi_{\text{int}} + \Pi_{\text{kin}} - \Pi_{\text{ext}}\,, \tag{28}$$

where the three contributions denote the Helmholtz free energy Π_{int}, the kinetic energy Π_{kin} and the external energy Π_{ext}, respectively. Based on the formulation of energy minimization by Francfort and Marigo (1998), the Helmholtz free energy contains elastic and fracture energy contributions in the form

$$\Pi_{\text{int}} = \int_{\mathcal{S}_0} \Psi\, \mathrm{d}A = \int_{\mathcal{S}_0} \Big[g(\phi)\Psi_{\text{el}}^{+} + \Psi_{\text{el}}^{-} + \Psi_{\text{frac}} \Big]\, \mathrm{d}A\,, \tag{29}$$

where Ψ denotes the Helmholtz free energy per reference area. Cracks resemble discontinuities in the deformation that are smeared out in the phase field formulation. Therefore, an indicator $\phi \in [0,1]$ is established that distinguishes between fully fractured, $\phi = 0$, and undamaged, $\phi = 1$, material. This field is referred to as the phase field or fracture field. Since it models the damage region, it is used to define the fracture energy appearing in Eq. (29). The higher order phase field model by Borden et al. (2014) is adopted here, which, expressed in variables of the present thin shell formulation, reads

$$\Psi_{\text{frac}} = \frac{\mathcal{G}_{\text{c}}}{4\ell_0}\left[(\phi-1)^2 + 2\ell_0^2\,\nabla_{\text{S}}\phi\cdot\nabla_{\text{S}}\phi + \ell_0^4\,(\Delta_{\text{S}}\phi)^2\right]. \tag{30}$$

The length scale parameter ℓ_0 [m] controls the support width of the transition zone: $\text{supp}(\phi) \sim \ell_0$. Borden et al. (2014) have shown that the one-dimensional phase field approximation of the crack surface $\Gamma = \{0\}$ has the form

$$\phi(x) = 1 - \exp\left(-\frac{|x|}{\ell_0}\right)\left(1 + \frac{|x|}{\ell_0}\right), \tag{31}$$

which is illustrated in Fig. 1.

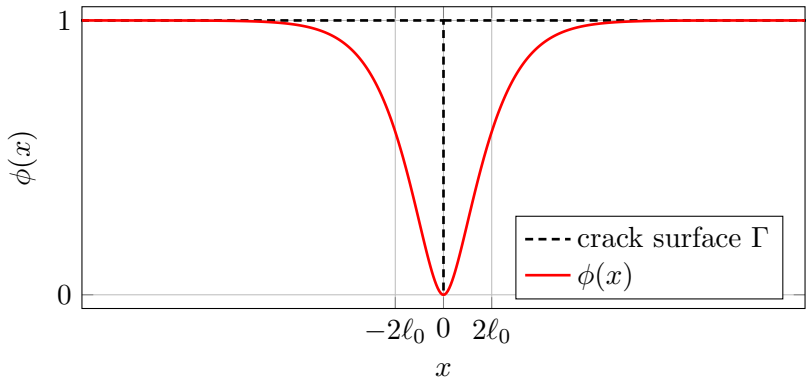

Figure 1: Phase field profile for the fourth-order theory of Borden et al. (2014). The crack surface $\Gamma = \{0\}$ is smoothed out by the function $\phi(x)$ in Eq. (31).

An additive energy split is required in which the elastic energy density is split into a part that contributes to crack evolution ('+') and a part that has no effect on crack growth ('−'): $\Psi_{\text{el}} = \Psi_{\text{el}}^{+} + \Psi_{\text{el}}^{-}$. The two contributions are also referred to as the positive and negative part of the elastic energy density. The split is further motivated and derived in Sec. 4.2.1. According to Eq. (29), the positive part of the elastic energy density Ψ_{el}^{+} is degraded through $g(\phi)$ along the damage regions. Here, it is assumed to take the form (Borden et al., 2016)

$$g(\phi) = (3-s)\phi^2 - (2-s)\phi^3, \tag{32}$$

where $s > 0$ describes the slope of $g(\phi)$ at $\phi = 1$. If $s = 0$, a surface without initial damage would fulfill the governing equation for crack evolution (60) for any deformation implying that crack nucleation would not occur. Thus, s is set to 10^{-4} (Borden et al., 2016) in all subsequent computations to allow crack nucleation in the absence of initial damage. Degradation functions with $g'(1) = 0$ could be used but they require a perturbation in the first Newton-Raphson iteration to allow for crack nucleation in sound materials (Kuhn et al., 2015).

4.2 Hyperelastic material model

The elastic energy density Ψ_{el} is taken as an additive composition of dilatational, deviatoric and bending energy densities in the form

$$\Psi_{\text{el}} = \underbrace{\Psi_{\text{dil}}(a_{\alpha\beta}) + \Psi_{\text{dev}}(a_{\alpha\beta})}_{\Psi_{\text{mem}}(a_{\alpha\beta})} + \Psi_{\text{bend}}(b_{\alpha\beta})\,, \tag{33}$$

where the first two terms describe the membrane part of Ψ_{el}. A Neo-Hookean surface material model (Sauer and Duong, 2017) with

$$\Psi_{\text{dil}} = \frac{K}{4}\big(J^2 - 1 - 2\,\ln J\big)\,, \tag{34}$$

and

$$\Psi_{\text{dev}} = \frac{G}{2}\big(I_1/J - 2\big)\,, \tag{35}$$

is used to model the isotropic in-plane constitutive response. K refers to the 2D bulk modulus and G to the 2D shear modulus. The bending response follows from the Koiter model (Ciarlet, 1993)

$$\Psi_{\text{bend}} = \frac{c}{2}\Big(b_{\alpha\beta} - B_{\alpha\beta}\Big)\Big(b_0^{\alpha\beta} - B^{\alpha\beta}\Big)\,, \tag{36}$$

with bending modulus c and $b_0^{\alpha\beta} := A^{\alpha\gamma} b_{\gamma\delta} A^{\beta\delta}$. Differentiating the Helmholtz free energy with respect to metric and curvature components, yields the stress and moment components

$$\begin{aligned} \tau^{\alpha\beta} &= 2\frac{\partial \Psi}{\partial a_{\alpha\beta}}\,, \\ M_0^{\alpha\beta} &= \frac{\partial \Psi}{\partial b_{\alpha\beta}}\,. \end{aligned} \tag{37}$$

Here, these components are given with respect to the reference configuration but they can be mapped to the current configuration by dividing the expressions in Eq. (37) by the surface stretch J. The individual derivatives for the material model in Eqs. (34), (35) and (36) read (Sauer and Duong, 2017; Zimmermann et al., 2019)

$$\begin{aligned} \tau^{\alpha\beta} &= \tau_{\text{dil}}^{\alpha\beta} + \tau_{\text{dev}}^{\alpha\beta}\,, \\ \tau_{\text{dil}}^{\alpha\beta} &= \frac{K}{2}(J^2 - 1)\, a^{\alpha\beta}\,, \\ \tau_{\text{dev}}^{\alpha\beta} &= \frac{G}{2J}(2A^{\alpha\beta} - I_1\, a^{\alpha\beta})\,, \\ M_0^{\alpha\beta} &= c\,(b_0^{\alpha\beta} - B^{\alpha\beta})\,. \end{aligned} \tag{38}$$

4.2.1 Split of the elastic energy density

Crack evolution shows anisotropic behavior since cracks will not propagate for every state of stress. To avoid cracking in compression an energy split is required as follows

$$\Psi_{\text{el}} = \Psi_{\text{el}}^{+} + \Psi_{\text{el}}^{-}\,, \tag{39}$$

where Ψ_{el}^{-} refers to the part of the elastic energy density that does not contribute to the fracture process. Amor et al. (2009) make use of a split into deviatoric and dilational parts in which

crack evolution is not permitted in volumetric compression but allowed in states of volumetric expansion and shear. In the work of Miehe et al. (2010a), a spectral decomposition of the strain tensor is introduced in which only positive strains contribute to the fracture process. Likewise, Kiendl et al. (2016) establish a spectral decomposition within a small deformation framework in plates and shells. They have outlined that it is not possible to consider a split into tension and compression as well as a split into membrane and bending contributions at the same time if such a spectral decomposition of the total strain is used. In our formulation, the elastic energy density is already split into membrane and bending parts according to Eq. (33) such that these terms can be decomposed separately

$$\Psi_{\text{el}}^{\pm} = \Psi_{\text{mem}}^{\pm} + \Psi_{\text{bend}}^{\pm} \,. \tag{40}$$

In the following, we show an example taken from Kiendl et al. (2016) that they use to motivate the need for a thickness integration for the energy split. We use their example to motivate the proposed split of the bending energy density. The strain distribution over the shell's thickness is illustrated in Fig. 2. The total strain $\tilde{\boldsymbol{E}} = \boldsymbol{E} - \xi \boldsymbol{K}$ with components $\tilde{E}_{\alpha\beta}$ and thickness coordinate $\xi \in \left[-\frac{T}{2}, \frac{T}{2}\right]$ can have both, positive and negative parts over the thickness T. It follows that there is a region of compression, which must not contribute to the fracture process. The membrane strains (due to the surface Green-Lagrange strain tensor $\boldsymbol{E}$) are purely positive in this example, whereas the strains associated with the curvature part are asymmetrically distributed around the mid-plane of the shell. Since Kiendl et al. (2016) are only interested in the tensile contributions, thickness effects for the elastic energy need to be considered to correctly distinguish between tensile and compressive contributions to the total strain. In contrast to this, the kinematical objects on the mid-plane include enough information for a suitable split of the membrane part. Subsequently, the individual splits of in-plane and out-of-plane parts are derived.

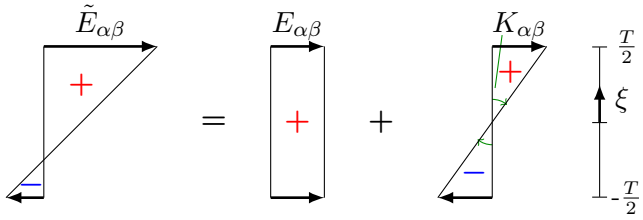

Figure 2: Strains over the shell's thickness (Kiendl et al., 2016). In this example, the membrane part shows purely positive strains, whereas the strains of the bending part are skew-symmetric around the mid-plane. If the negative strains are not supposed to contribute to crack growth, the strain distribution over the thickness has to be taken into consideration. Kiendl et al. (2016) introduce a thickness integration and split the total strain with a spectral decomposition. Their work motivates the necessity of our thickness integration (cf. Eq. (44)).

As already mentioned, a spectral decomposition of the strain tensor is not suitable in the present formulation since our elastic energy density is given as a sum of membrane and bending contributions. Instead, we follow the decomposition introduced by Amor et al. (2009), which has also been used by e.g. Ambati et al. (2016) and Borden et al. (2016). Corresponding to whether the surface stretch J is greater than/equal to 1 or smaller than 1, the dilatational part will contribute to crack growth or not. The split of the membrane energy density required in Eq. (40) then yields

$$\Psi_{\text{mem}}^{+} = \begin{cases} \Psi_{\text{dev}} + \Psi_{\text{dil}} \,, & J \geq 1 \\ \Psi_{\text{dev}} \,, & J < 1 \end{cases} , \qquad \Psi_{\text{mem}}^{-} = \begin{cases} 0 \,, & J \geq 1 \\ \Psi_{\text{dil}} \,, & J < 1 \end{cases} . \tag{41}$$

Thus, crack evolution is not permitted in states of volumetric compression ($J < 1$) but allowed in states of pure shear ($J = 1$) or volumetric expansion ($J > 1$). For instance Ambati et al. (2015) have shown that this split works well for fracture prediction, but we note that a suitable split of the deviatoric energy density might be missing in Eq. (41).
The thickness has to be taken into account in order to obtain a suitable split of the bending energy density in Eq. (36). This is obtained from following relation (Duong et al., 2017)

$$\Psi_{\text{bend}} = \int_{-\frac{T}{2}}^{\frac{T}{2}} \tilde{\Psi}_{\text{bend}}(\xi)\, \mathrm{d}\xi\,, \tag{42}$$

where the corresponding three-dimensional constitutive model[2] is given by

$$\tilde{\Psi}_{\text{bend}}\left(\boldsymbol{K}, \xi, T\right) = \xi^2 \frac{12}{T^3} \frac{c}{2} \operatorname{tr}\left(\boldsymbol{K}^2\right). \tag{43}$$

The split of Ψ_{bend} is then modeled as

$$\Psi^{\pm}_{\text{bend}} = \int_{-\frac{T}{2}}^{\frac{T}{2}} \tilde{\Psi}^{\pm}_{\text{bend}}(\xi)\, \mathrm{d}\xi\,. \tag{44}$$

Still, Eq. (43) has to be additively decomposed according to $\tilde{\Psi}_{\text{bend}} = \tilde{\Psi}^{+}_{\text{bend}} + \tilde{\Psi}^{-}_{\text{bend}}$. Already in Eq. (41) the surface stretch at the mid-plane has been employed as an indicator for a possible contribution to the fracture process. The surface stretch of other shell layers is obtained in analogy to Eq. (12.2) as

$$\tilde{J} = \sqrt{\det[\tilde{A}^{\alpha\beta}]\det[\tilde{a}_{\alpha\beta}]}\,. \tag{45}$$

The metrics $\tilde{A}^{\alpha\beta}$ and $\tilde{a}_{\alpha\beta}$ follow from the tangent vectors $\tilde{\boldsymbol{A}}_\alpha$ and $\tilde{\boldsymbol{a}}_\alpha$ of the shell layer at points $\boldsymbol{x} + \xi\, \boldsymbol{n}$ and $\boldsymbol{X} + \xi\, \boldsymbol{N}$, respectively (Duong et al., 2017). The split of $\tilde{\Psi}_{\text{bend}}$ then follows as

$$\tilde{\Psi}^{+}_{\text{bend}}(\xi) = \begin{cases} \xi^2 \dfrac{12}{T^3} \dfrac{c}{2} \operatorname{tr}\left(\boldsymbol{K}^2\right), & \tilde{J}(\xi) \geq 1 \\ 0\,, & \tilde{J}(\xi) < 1 \end{cases}, \quad \tilde{\Psi}^{-}_{\text{bend}}(\xi) = \begin{cases} 0\,, & \tilde{J}(\xi) \geq 1 \\ \xi^2 \dfrac{12}{T^3} \dfrac{c}{2} \operatorname{tr}\left(\boldsymbol{K}^2\right), & \tilde{J}(\xi) < 1 \end{cases}. \tag{46}$$

Based on Eq. (44), the decomposition of the bending energy density follows from thickness integration of Eq. (46). Thickness integration is performed numerically using Gaussian quadrature. We note that an analytical integration of Eq. (46) over the thickness is in general not possible due to the strong nonlinear dependence of the surface stretch $\tilde{J}$ on ξ. But there are two special cases for which Eq. (44) can be solved analytically, i.e.

$$\tilde{J}(\xi) \geq 1\,,\ \forall \xi \in \left[-\frac{T}{2}, \frac{T}{2}\right]: \quad \Psi^{+}_{\text{bend}} = \frac{c}{2}\left(b_{\alpha\beta} - B_{\alpha\beta}\right)\left(b_0^{\alpha\beta} - B^{\alpha\beta}\right), \quad \Psi^{-}_{\text{bend}} = 0\,, \tag{47}$$

and

$$\tilde{J}(\xi) < 1\,,\ \forall \xi \in \left[-\frac{T}{2}, \frac{T}{2}\right]: \quad \Psi^{+}_{\text{bend}} = 0\,, \quad \Psi^{-}_{\text{bend}} = \frac{c}{2}\left(b_{\alpha\beta} - B_{\alpha\beta}\right)\left(b_0^{\alpha\beta} - B^{\alpha\beta}\right). \tag{48}$$

These relations can then be used for an efficient FE implementation.

[2] This is a part of the Saint Venant-Kirchhoff model, see Duong et al. (2017).

4.2.2 Stresses and moments

Based on the energy split from the previous section, the stress and moment components follow. In the reference configuration, the stress components read

$$\tau^{\alpha\beta} = g(\phi)\,\tau_+^{\alpha\beta} + \tau_-^{\alpha\beta}\,, \tag{49}$$

with the individual contributions

$$\tau_+^{\alpha\beta} = \begin{cases} \tau_{\text{dev}}^{\alpha\beta} + \tau_{\text{dil}}^{\alpha\beta}\,, & J \geq 1 \\ \tau_{\text{dev}}^{\alpha\beta}\,, & J < 1 \end{cases}\,, \qquad \tau_-^{\alpha\beta} = \begin{cases} 0\,, & J \geq 1 \\ \tau_{\text{dil}}^{\alpha\beta}\,, & J < 1 \end{cases}\,. \tag{50}$$

The individual contributions in Eq. (50) are given in Eq. (38.2)-(38.3). The moment components read

$$M_0^{\alpha\beta} = g(\phi)\,M_{0,+}^{\alpha\beta} + M_{0,-}^{\alpha\beta}\,, \tag{51}$$

where the contributions are computed based on thickness integration via

$$M_{0,\pm}^{\alpha\beta} = \int_{-\frac{T}{2}}^{\frac{T}{2}} \tilde{M}_{0,\pm}^{\alpha\beta}(\xi)\,\mathrm{d}\xi\,, \tag{52}$$

with

$$\tilde{M}_{0,+}^{\alpha\beta}(\xi) = \begin{cases} \dfrac{\partial \tilde{\Psi}_{\text{bend}}(\xi)}{\partial b_{\alpha\beta}}\,, & \tilde{J}(\xi) \geq 1 \\ 0\,, & \tilde{J}(\xi) < 1 \end{cases} \qquad \tilde{M}_{0,-}^{\alpha\beta}(\xi) = \begin{cases} 0\,, & \tilde{J}(\xi) \geq 1 \\ \dfrac{\partial \tilde{\Psi}_{\text{bend}}(\xi)}{\partial b_{\alpha\beta}}\,, & \tilde{J}(\xi) < 1 \end{cases}\,. \tag{53}$$

The required derivative in Eq. (53) is given by

$$\frac{\partial \tilde{\Psi}_{\text{bend}}(\xi)}{\partial b_{\alpha\beta}} = \xi^2 \frac{12}{T^3} c\,(b_0^{\alpha\beta} - B^{\alpha\beta})\,, \tag{54}$$

with $b_0^{\alpha\beta} = A^{\alpha\gamma} b_{\gamma\delta} A^{\beta\delta}$. We note that we have assumed that the order of integration $\int_{-T/2}^{T/2}(\cdot)\,\mathrm{d}\xi$ and differentiation $\partial(\cdot)/\partial b_{\alpha\beta}$ can be exchanged.

4.3 Irreversible fracture

Crack evolution is an irreversible process since cracks cannot heal. Thus, the irreversibility condition $\Gamma(t+\Delta t) \subseteq \Gamma(t)\,,\ \forall \Delta t > 0$ where Γ is the crack surface needs to be enforced algorithmically. As described in Gerasimov and De Lorenzis (2018), several methods exist to enforce this constraint within a phase field model for fracture. The constraint is rewritten in terms of the phase field as $\phi(\boldsymbol{x}, t+\Delta t) \leq \phi(\boldsymbol{x}, t)\,,\ \forall \Delta t > 0$. In our work we make use of a history field

$$\mathcal{H}(\boldsymbol{x}, t) := \max_{\tau \in [0,t]} \Psi_{\text{el}}^{+}(\boldsymbol{x}, \tau)\,, \tag{55}$$

which keeps track of the fracture contributing part of the elastic energy density (Miehe et al., 2010a). Ψ_{el}^{+} in Eq. (29) is then replaced by the history field $\mathcal{H}$. Complex initial crack patterns can also be realized by means of the history field (Borden et al., 2012).

4.4 Euler-Lagrange equation and strong form

Combining Eqs. (28)–(29) and (55), the total energy in the system follows as

$$\Pi := \int_{\mathcal{S}_0} \Big[g(\phi)\mathcal{H} + \Psi_{\text{el}}^{-} + \Psi_{\text{frac}}(\phi) \Big] \, \mathrm{d}A - \Pi_{\text{ext}} + \Pi_{\text{kin}} \, . \tag{56}$$

The kinetic energy Π_{kin} and the potential energy Π_{ext} do not depend on ϕ. The elastic energy density occurring from volumetric compression Ψ_{el}^{-} does not contribute to crack propagation and is thus, not degraded in the domain of fracture. In contrast to this, $\mathcal{H}$ is degraded by the degradation function $g(\phi)$, but is not a function of ϕ itself. Only the energy density Ψ_{frac} depends on ϕ, as seen in Eq. (30). The minimization of the energy functional can be expressed by setting its variation to zero: $\delta\Pi = 0$. The latter is solved by making use of the Euler-Lagrange equation, which then leads to the strong form for the phase field's evolution. Given the Helmholtz free energy per reference area $\Psi = \Psi(\phi, \phi_{,\alpha}, \phi_{;\alpha\beta})$, its variation reads

$$\delta\Psi = \frac{\partial \Psi}{\partial \phi} \, \delta\phi + \frac{\partial \Psi}{\partial \phi_{,\alpha}} \, \delta(\phi_{,\alpha}) + \frac{\partial \Psi}{\partial \phi_{;\alpha\beta}} \, \delta(\phi_{;\alpha\beta}) \, . \tag{57}$$

Integration over the reference surface and applying integration by parts twice, yields

$$\int_{\mathcal{S}_0} \delta\Psi \mathrm{d}A = \int_{\mathcal{S}_0} \left(\frac{\partial \Psi}{\partial \phi} - \left(\frac{\partial \Psi}{\partial \phi_{,\alpha}} \right)_{,\alpha} + \left(\frac{\partial \Psi}{\partial \phi_{;\alpha\beta}} \right)_{;\alpha\beta} \right) \delta\phi \, \mathrm{d}A + \text{boundary terms} \, . \tag{58}$$

The boundary terms vanish by choosing appropriate boundary conditions for $\delta\phi$. Boundary conditions for ϕ are given in Eq. (63). The energy minimization problem now reads $\delta\Psi = 0$. Since Eq. (58) holds true for all $\delta\phi$, the Euler-Lagrange equation follows from applying the fundamental lemma of variational calculus, yielding

$$\frac{\partial \Psi}{\partial \phi} - \left(\frac{\partial \Psi}{\partial \phi_{,\alpha}} \right)_{,\alpha} + \left(\frac{\partial \Psi}{\partial \phi_{;\alpha\beta}} \right)_{;\alpha\beta} = 0 \, . \tag{59}$$

Inserting the Helmholtz free energy per reference area described in Sec. 4 yields the strong form of the phase field fracture equation

$$\frac{2\ell_0}{\mathcal{G}_{\text{c}}} g'(\phi) \, \mathcal{H} + \phi - 1 - 2\,\ell_0^2 \, A^{\alpha\beta} \, \phi_{,\alpha\beta} + \ell_0^4 \, A^{\gamma\delta} \big(A^{\alpha\beta} \, \phi_{;\alpha\beta} \big)_{;\gamma\delta} = 0 \, , \quad \forall \, \phi \in \mathcal{S} \, , \tag{60}$$

with $g'(\phi) = \partial g(\phi) / \partial \phi$.

4.5 Weak form for the phase field fracture equation

Integrating Eq. (57) over the domain $\mathcal{S}_0$, the weak form for the phase field fracture equation becomes

$$\int_{\mathcal{S}_0} \delta\phi \, f(\phi) \, \mathrm{d}A + \int_{\mathcal{S}_0} \nabla_{\text{S}}(\delta\phi) \cdot 2\ell_0^2 \, \nabla_{\text{S}}\phi \, \mathrm{d}A + \int_{\mathcal{S}_0} \Delta_{\text{S}}(\delta\phi) \, \ell_0^4 \, \Delta_{\text{S}}\phi \, \mathrm{d}A = 0 \, , \quad \forall \, \delta\phi \in \mathcal{V} \, , \tag{61}$$

with

$$f(\phi) := \frac{2\ell_0}{\mathcal{G}_{\text{c}}} g'(\phi)\mathcal{H} + \phi - 1 \, , \tag{62}$$

and the space of suitable test functions $\mathcal{V} = \big\{ \delta\phi \in \mathcal{H}^2\big(\mathcal{S}(\phi, t)\big) \big\}$. The boundary terms arising during the derivation of Eq. (61) vanish due to the choice of the following boundary conditions

$$\begin{aligned} \Delta_{\text{S}}\phi &= 0 \, , \\ \nabla_{\text{S}}\big(\ell_0^4 \, \Delta_{\text{S}}\phi - 2\ell_0^2 \, \phi \big) \cdot \boldsymbol{n} &= 0 \, , \end{aligned} \tag{63}$$

for all $\phi(\boldsymbol{x}, t)$ with $\boldsymbol{x} \in \partial\mathcal{S}$.

5 Discretization of the coupled problem

This section presents the monolithic discretization of the coupled system consisting of the thin shell equation, the phase field evolution equation and their interaction. For the numerical examples presented in Sec. 6 the shell surface is discretized by isogeometric finite elements (Hughes et al., 2005) since the high order operators of the coupled weak form require at least global C^1-continuity. For the spatial discretization, LR NURBS (Zimmermann and Sauer, 2017) are employed to construct locally refined meshes in the domain of fracture. For the temporal discretization, the generalized-α scheme of Chung and Hulbert (1993) is used.

5.1 Adaptive local surface refinement

5.1.1 LR NURBS

The fundamental work of Dokken et al. (2013) and their introduction of LR B-splines has been extended to LR NURBS by Zimmermann and Sauer (2017). A knot vector Ξ of size $n+p+1$ defines n linearly independent basis functions of order p. In the framework of LR NURBS, the global knot vector $\Xi = [\xi_1, ..., \xi_{n+p+1}]$ is split into local knot vectors $\Xi_i = [\xi_i, ..., \xi_{i+p+1}]$ $(i = 1, \dots, n)$ to represent local parameter domains. Each of these local knot vectors defines a single basis function. By construction the basis function has minimal support on the local knot vector. Local refinement is performed by mesh line extensions in the parameter space. This includes insertion of new mesh lines, joining or elongation of existing ones or an increase of their multiplicity. The latter results in a decrease of continuity. Local refinement is based on knot insertion (Dokken et al., 2013), which is described for LR NURBS in the work of Zimmermann and Sauer (2017). LR NURBS inherit several mathematical properties from standard NURBS: The basis forms a partition of unity, it is non-negative and the geometry lies within the convex hull of the control points.

5.1.2 Criteria for surface refinement

An accurate phase field approximation of the discontinuity across the crack is achieved by using a small length scale parameter ℓ_0. This requires a highly resolved finite element mesh in the vicinity of the crack. The phase field ϕ is used as an indicator for refinement: As soon as a control point's phase field value is smaller or equal to ϕ_{bound}, all elements that lie in the support domain of the corresponding basis functions will be flagged for refinement. If these elements are not yet refined up to a prescribed refinement depth, mesh line extensions are performed until the desired refinement depth is achieved. The latter can be computed based on the element areas. This refinement strategy is called *Structured mesh* (Johannessen et al., 2014) and is illustrated in Fig. 3. The blue shaded area in the parameter domain resembles the support domain of a basis function, that is flagged for refinement. The dashed red lines are then inserted into the parameter domain. This is done recursively for all newly created basis functions up to the prescribed refinement depth. The refinement based on mesh line insertion and modification is described in Sec. 5.1.1. We have found $\phi_{\text{bound}} = 0.975$ to be a suitable choice for the threshold. We note that in the case of crack nucleation, the last time step needs to be recomputed to ensure crack initiation in a region of highly resolved mesh.

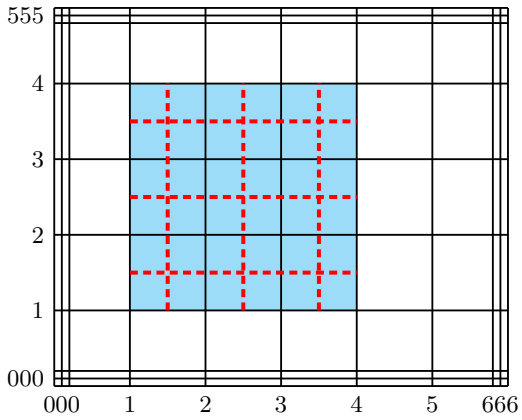

Figure 3: Refinement strategy *Structured mesh*: The blue shaded area resembles the support domain of a basis function, that is flagged for refinement. The dashed red lines are then inserted into the parameter domain. (Johannessen et al., 2014)

5.2 Spatial discretization of primary fields

Subsequently, the finite element approximations of the surface deformation and the phase field are described. It follows the work of Sauer et al. (2014), Sauer et al. (2017), Duong et al. (2017) and Zimmermann et al. (2019). Let n_e denote the number of spline basis functions on parametric element Ω_e. They are numbered with global indices $i_1, \dots, i_{n_e}$. The surface representation follows from this as

$$\boldsymbol{X}^h = \mathbf{N}\,\mathbf{X}_e\,, \quad \text{and} \quad \boldsymbol{x}^h = \mathbf{N}\,\mathbf{x}_e\,, \tag{64}$$

for the reference and current surface, respectively. The corresponding shape function array reads

$$\mathbf{N} := [N_{i_1}\mathbf{1},\, N_{i_2}\mathbf{1},\, ...,\, N_{i_{n_e}}\mathbf{1}]\,. \tag{65}$$

Here, the element-level vectors are denoted $\mathbf{X}_e$ and $\mathbf{x}_e$ and $\mathbf{1}$ refers to the (3×3) identity matrix. Likewise, the phase field is approximated via

$$\phi^h = \bar{\mathbf{N}}\,\boldsymbol{\phi}_e\,, \tag{66}$$

with element-level nodal values $\boldsymbol{\phi}_e$ and shape function array

$$\bar{\mathbf{N}} := [N_{i_1},\, N_{i_2},\, ...,\, N_{i_{n_e}}]\,. \tag{67}$$

The local vectors contain the nodal values with indices $i_1, \dots, i_{n_e}$. These can be extracted from the global ones $\mathbf{X}$, $\mathbf{x}$ and $\boldsymbol{\phi}$ which contain all nodal values. In analogy to Eqs. (64) and (66), the corresponding variations read

$$\delta\boldsymbol{X}^h = \mathbf{N}\,\delta\mathbf{X}_e\,, \quad \text{and} \quad \delta\boldsymbol{x}^h = \mathbf{N}\,\delta\mathbf{x}_e\,, \tag{68}$$

and

$$\delta\phi^h = \bar{\mathbf{N}}\,\delta\boldsymbol{\phi}_e\,. \tag{69}$$

Based on Eq. (64), the discretized tangent vectors follow as

$$\boldsymbol{A}_\alpha^h = \mathbf{N}_{,\alpha}\,\mathbf{X}_e\,, \quad \text{and} \quad \boldsymbol{a}_\alpha^h = \mathbf{N}_{,\alpha}\,\mathbf{x}_e\,, \tag{70}$$

with $\mathbf{N}_{,\alpha} := \partial\mathbf{N}/\partial\xi^\alpha$. From this, the discretized normals $\boldsymbol{n}^h$ and $\boldsymbol{N}^h$ follow according to Eq. (4).[3] The metric and curvature tensor components in the reference configuration are then given by

$$A^h_{\alpha\beta} = \mathbf{X}_e^{\mathrm{T}}\,\mathbf{N}_{,\alpha}^{\mathrm{T}}\,\mathbf{N}_{,\beta}\,\mathbf{X}_e\,, \quad \text{and} \quad B^h_{\alpha\beta} = \boldsymbol{N}^h \cdot \mathbf{N}_{,\alpha\beta}\,\mathbf{X}_e\,, \tag{71}$$

and similarly for the current surface

$$a^h_{\alpha\beta} = \mathbf{x}_e^{\mathrm{T}}\,\mathbf{N}_{,\alpha}^{\mathrm{T}}\,\mathbf{N}_{,\beta}\,\mathbf{x}_e\,, \quad \text{and} \quad b^h_{\alpha\beta} = \boldsymbol{n}^h \cdot \mathbf{N}_{,\alpha\beta}\,\mathbf{x}_e\,. \tag{72}$$

From this, the contra-variant metrics $[A_h^{\alpha\beta}] = [A^h_{\alpha\beta}]^{-1}$ and $[a_h^{\alpha\beta}] = [a^h_{\alpha\beta}]^{-1}$ follow. In analogy, the discretized variations of the surface metric and curvature are given by

$$\delta a^h_{\alpha\beta} = \delta\mathbf{x}_e^{\mathrm{T}}\big(\mathbf{N}_{,\alpha}^{\mathrm{T}}\,\mathbf{N}_{,\beta} + \mathbf{N}_{,\beta}^{\mathrm{T}}\,\mathbf{N}_{,\alpha}\big)\,\mathbf{x}_e\,, \quad \text{and} \quad \delta b^h_{\alpha\beta} = \delta\mathbf{x}_e^{\mathrm{T}}\,\mathbf{N}_{;\alpha\beta}^{\mathrm{T}}\,\boldsymbol{n}^h\,, \tag{73}$$

with

$$\mathbf{N}_{;\alpha\beta} := \mathbf{N}_{,\alpha\beta} - \Gamma^\gamma_{\alpha\beta}\,\mathbf{N}_{,\gamma}\,, \tag{74}$$

and discretized Christoffel symbols (cf. Sec. 2.1)

$$\Gamma^\gamma_{\alpha\beta} = \mathbf{x}_e^{\mathrm{T}}\,\mathbf{N}_{,\alpha\beta}^{\mathrm{T}}\,a_h^{\gamma\delta}\,\mathbf{N}_{,\delta}\,\mathbf{x}_e\,. \tag{75}$$

Using Eqs. (7), (8) and (66), the derivatives of the phase field follow as

$$\begin{aligned}
\phi^h_{;\alpha} &= \bar{\mathbf{N}}_{,\alpha}\,\boldsymbol{\phi}_e\,,\\
\nabla_{\mathrm{S}}\phi^h &= \boldsymbol{A}_h^\alpha\,\bar{\mathbf{N}}_{,\alpha}\,\boldsymbol{\phi}_e\,,\\
\nabla_{\mathrm{S}}\delta\phi^h &= \boldsymbol{A}_h^\alpha\,\bar{\mathbf{N}}_{,\alpha}\,\delta\boldsymbol{\phi}_e\,,\\
\Delta_{\mathrm{S}}\phi^h &= \Delta_{\mathrm{S}}\bar{\mathbf{N}}\,\boldsymbol{\phi}_e\,,\\
\Delta_{\mathrm{S}}\delta\phi^h &= \Delta_{\mathrm{S}}\bar{\mathbf{N}}\,\delta\boldsymbol{\phi}_e\,,
\end{aligned} \tag{76}$$

with $\boldsymbol{A}_h^\alpha = A_h^{\alpha\beta}\boldsymbol{A}^h_\beta$ and $\bar{\mathbf{N}}_{,\alpha} := \partial\bar{\mathbf{N}}/\partial\xi^\alpha$ and

$$\Delta_{\mathrm{S}}\bar{\mathbf{N}} := A_h^{\alpha\beta}\,\hat{\bar{\mathbf{N}}}_{;\alpha\beta}\,, \tag{77}$$

where

$$\hat{\bar{\mathbf{N}}}_{;\alpha\beta} = \bar{\mathbf{N}}_{,\alpha\beta} - \hat{\Gamma}^\gamma_{\alpha\beta}\,\bar{\mathbf{N}}_{,\gamma}\,. \tag{78}$$

Note that here the discretized Christoffel symbols need to be taken from the reference surface (cf. Sec. 2.1), i.e.

$$\hat{\Gamma}^\gamma_{\alpha\beta} = \mathbf{X}_e^{\mathrm{T}}\,\mathbf{N}_{,\alpha\beta}^{\mathrm{T}}\,A_h^{\gamma\delta}\,\mathbf{N}_{,\delta}\,\mathbf{X}_e\,. \tag{79}$$

5.3 Spatial discretization of the mechanical weak form

Inserting the above approximations into Eq. (24) yields the discretized mechanical weak form

$$\delta\mathbf{x}^{\mathrm{T}}\left[\mathbf{f}_{\mathrm{kin}} + \mathbf{f}_{\mathrm{int}} - \mathbf{f}_{\mathrm{ext}}\right] = 0\,, \quad \forall\ \delta\mathbf{x} \in \mathcal{U}^h\,, \tag{80}$$

with global force vectors $\mathbf{f}_{\mathrm{kin}}$, $\mathbf{f}_{\mathrm{int}}$ and $\mathbf{f}_{\mathrm{ext}}$. These are assembled from their respective elemental contributions

$$\begin{aligned}
\mathbf{f}^e_{\mathrm{kin}} &:= \mathbf{m}_e\,\ddot{\mathbf{x}}_e\,, \quad \mathbf{m}_e := \int_{\Omega^e} \rho\,\mathbf{N}^{\mathrm{T}}\mathbf{N}\,\mathrm{d}a\,,\\
\mathbf{f}^e_{\mathrm{int}} &:= \int_{\Omega^e}\Big(g(\phi^h)\,\sigma_+^{\alpha\beta} + \sigma_-^{\alpha\beta}\Big)\,\mathbf{N}_{,\alpha}^{\mathrm{T}}\,\boldsymbol{a}^h_\beta\,\mathrm{d}a + \int_{\Omega^e}\Big(g(\phi^h)\,M_+^{\alpha\beta} + M_-^{\alpha\beta}\Big)\,\mathbf{N}_{;\alpha\beta}^{\mathrm{T}}\,\boldsymbol{n}^h\,\mathrm{d}a\,,\\
\mathbf{f}^e_{\mathrm{ext}} &:= \int_{\Omega^e}\mathbf{N}^{\mathrm{T}}\,p(\phi)\,\boldsymbol{n}^h\,\mathrm{d}a + \int_{\Omega^e}\mathbf{N}^{\mathrm{T}}\,f^\alpha\,\boldsymbol{a}^h_\alpha\,\mathrm{d}a\,.
\end{aligned} \tag{81}$$

[3] To avoid confusion, we write discrete arrays, such as the shape function array $\mathbf{N}$, in roman font, whereas continuous tensors, such as the normal vector $\boldsymbol{N}$, are written in italic font.

The terms $\sigma_{\pm}^{\alpha\beta}$ and $M_{\pm}^{\alpha\beta}$ are given by the energy split outlined in Sec. 4.2.1. In $\mathbf{f}_{\text{ext}}^{e}$ we have taken the boundary loads $\boldsymbol{T}$ and $\boldsymbol{M}$ acting on $\partial\mathcal{S}$ as zero. The extension to boundary loads can be found in Duong et al. (2017). Apart from the dependence on $\mathbf{x}_e$, the force $\mathbf{f}_{\text{int}}^{e}$ depends on $\boldsymbol{\phi}_e$ through the degradation of $\sigma_{+}^{\alpha\beta}$ and $M_{+}^{\alpha\beta}$ by $g(\phi^h)$.
From a physical point of view the load-bearing capability vanishes in fully damaged regions where $\phi = 0$. Thus, no pressure can act on the corresponding regions. We account for this by scaling the pressure linearly based on the phase field, i,.e.

$$p(\phi) = \phi\,\bar{p}\,, \tag{82}$$

with $\bar{p}$ denoting the pressure imposed on undamaged elements. Huge deformations and distorted elements at regions of full damage are prevented by means of the pressure function in Eq. (82). Putting everything together, the resulting equation system for the free nodes[4] reads

$$\mathbf{f}(\mathbf{x},\boldsymbol{\phi}) = \mathbf{M}\,\ddot{\mathbf{x}} + \mathbf{f}_{\text{int}}(\mathbf{x},\boldsymbol{\phi}) - \mathbf{f}_{\text{ext}}(\mathbf{x},\boldsymbol{\phi}) = \mathbf{0}\,. \tag{83}$$

The global mass matrix $\mathbf{M}$ is assembled from the elemental contributions $\mathbf{m}_e$.

5.4 Spatial discretization of the phase field

Inserting the approximations from Sec. 5.2 into the discretized weak form of Eq. (61) yields

$$\delta\boldsymbol{\phi}^{\mathrm{T}}\left[\bar{\mathbf{f}}_{\text{kin}} + \bar{\mathbf{f}}_{\text{int}} - \bar{\mathbf{f}}_{\text{ext}}\right] = 0\,, \quad \forall\,\delta\boldsymbol{\phi} \in \mathcal{V}^h\,, \tag{84}$$

where the global vectors $\bar{\mathbf{f}}_{\text{kin}}$, $\bar{\mathbf{f}}_{\text{int}}$, $\bar{\mathbf{f}}_{\text{ext}}$ and $\bar{\mathbf{f}}_{\text{ir}}$ follow from the assembly of their corresponding elemental contributions

$$\begin{aligned}
\bar{\mathbf{f}}_{\text{kin}}^{e} &:= \mathbf{0}\,,\\
\bar{\mathbf{f}}_{\text{int}}^{e} &:= \bar{\mathbf{k}}_0^{e}\,\boldsymbol{\phi}_e + \bar{\mathbf{f}}_{\text{el}}^{e} - \bar{\mathbf{f}}_0^{e}\,, \quad \bar{\mathbf{k}}_0^{e} := \int_{\Omega_0^e}\left[\bar{\mathbf{N}}^{\mathrm{T}}\bar{\mathbf{N}} + \bar{\mathbf{N}}_{,\alpha}^{\mathrm{T}}\,2\ell_0^2\,A^{\alpha\beta}\,\bar{\mathbf{N}}_{,\beta} + \Delta_{\mathrm{S}}\bar{\mathbf{N}}^{\mathrm{T}}\,\ell_0^4\,\Delta_{\mathrm{S}}\bar{\mathbf{N}}\right]\mathrm{d}A\,,\\
\bar{\mathbf{f}}_{\text{el}}^{e} &:= \int_{\Omega_0^e}\bar{\mathbf{N}}^{\mathrm{T}}\frac{2\ell_0}{\mathcal{G}_{\mathrm{c}}}g'(\phi)\mathcal{H}\,\mathrm{d}A\,,\\
\bar{\mathbf{f}}_{0}^{e} &:= \int_{\Omega_0^e}\bar{\mathbf{N}}^{\mathrm{T}}\,\mathrm{d}A\,,\\
\bar{\mathbf{f}}_{\text{ext}}^{e} &:= \mathbf{0}\,.
\end{aligned} \tag{85}$$

Apart from the dependence on $\boldsymbol{\phi}_e$, these expressions depend on $\mathbf{x}_e$ through $\mathcal{H}$. The resulting equations at the free nodes simplify to

$$\bar{\mathbf{f}}(\mathbf{x},\boldsymbol{\phi}) = \bar{\mathbf{f}}_{\text{int}}(\mathbf{x},\boldsymbol{\phi}) = \mathbf{0}\,. \tag{86}$$

5.5 Temporal discretization

5.5.1 Generalized-α method

The fully implicit generalized-α method of Chung and Hulbert (1993) is used as a monolithic time integration scheme. Given the quantities $(\mathbf{x}_n, \dot{\mathbf{x}}_n, \ddot{\mathbf{x}}_n, \boldsymbol{\phi}_n)$ at time t_n, the new values

[4] The free nodes refer to the degrees of freedom, which are not given by boundary conditions.

$(\mathbf{x}_{n+1}, \dot{\mathbf{x}}_{n+1}, \ddot{\mathbf{x}}_{n+1}, \boldsymbol{\phi}_{n+1})$ at time t_{n+1} need to be found. Additionally, equilibrium has to be fulfilled at intermediate states $(\mathbf{x}_{n+\alpha_\mathrm{f}}, \dot{\mathbf{x}}_{n+\alpha_\mathrm{f}}, \ddot{\mathbf{x}}_{n+\alpha_\mathrm{m}}, \boldsymbol{\phi}_{n+1})$, i.e.

$$\begin{bmatrix} \mathbf{f}\left(\mathbf{x}_{n+\alpha_\mathrm{f}}, \ddot{\mathbf{x}}_{n+\alpha_\mathrm{m}}, \boldsymbol{\phi}_{n+1}\right) \\ \bar{\mathbf{f}}\left(\mathbf{x}_{n+\alpha_\mathrm{f}}, \boldsymbol{\phi}_{n+1}\right) \end{bmatrix} = \mathbf{0}\,. \tag{87}$$

The complete scheme has been described in the work of Zimmermann et al. (2019). Since there are no temporal derivatives of the phase field in our framework, the corresponding equations simplify as outlined in Appendix A.

5.5.2 Adaptive time-stepping

The time step size should be chosen sufficiently small so that the crack does not propagate across too many elements in one time step. In contrast to this, large time steps can be used in cases of no crack propagation. This motivates the adaptive adjustment of the time step size. Since the phase field is not time-dependent, we cannot apply the adaptive time stepping scheme from Zimmermann et al. (2019). We therefore follow the subsequent approach: The need for smaller or the possibility of larger time steps can be indicated by the required number of Newton-Raphson iterations n_NR during the last iteration, as for instance done by Schlüter et al. (2014). We adjust the new time step size at time step $n+1$ as

$$\Delta t_{n+1} = \begin{cases} 1.5\,\Delta t_n\,, & n_\mathrm{NR} < 4 \\ 1.1\,\Delta t_n\,, & n_\mathrm{NR} = 4 \\ 0.5\,\Delta t_n\,, & n_\mathrm{NR} > 4 \\ 0.2\,\Delta t_n\,, & \text{local spatial refinement} \end{cases}\,. \tag{88}$$

The coefficients in Eq. (88) have been chosen based on the numerical examples presented in Sec. 6. Note that the time step size is also reduced after each spatial refinement step to ensure good convergence behavior. If not specified otherwise, a maximum time step size $\Delta t_\mathrm{max} = 0.1\,T_0$ and the initial time step size $\Delta t_0 = 10^{-6}\,T_0$ have been used for the numerical results[5].

5.6 Stabilization of jump conditions

In Eqs. (46) and (52) and in the corresponding linearizations (cf. Appendix B), integrals of the form

$$\int_{-\frac{T}{2}}^{\frac{T}{2}} \xi^2\,\chi\big(\tilde{J}(\xi)\big)\,\mathrm{d}\xi\,, \quad \text{with} \quad \chi\big(\tilde{J}(\xi)\big) = \begin{cases} 1, & \tilde{J}(\xi) \geq 1 \\ 0, & \tilde{J}(\xi) < 1 \end{cases}\,, \tag{89}$$

have to be computed. In the numerical examples presented in Sec. 6, we have observed that the jump function $\chi\big(\tilde{J}(\xi)\big)$ leads to convergence problems in which the Newton-Raphson iteration may alternate between different states. This occurs when the surface stretch $\tilde{J}(\xi)$ has values close to one so that $\chi\big(\tilde{J}(\xi)\big)$ may change its value after a Newton-Raphson update. We have tested two strategies to avoid these convergence problems: At first, an active set strategy can be employed. During a Newton-Raphson iteration the expressions in Eq. (89) are kept constant and the coupled system is solved for these values. Afterwards, the expressions are recomputed and another Newton-Raphson iteration is performed. This active set iteration is performed until either there is no change in the active set (the integral expressions), a maximum number of active set iterations is reached or the solution alternates again between different states. Since

[5] T_0 refers to a reference time used to obtain a dimensionless formulation, see Sec. 5.7

this strategy introduces another iteration it can increase the computational effort significantly. We thus propose another approach in which we smooth the discontinuity in $\chi\big(\tilde{J}(\xi)\big)$ by

$$\hat{\chi}\big(\tilde{J}(\xi)\big) := \frac{1}{1 + e^{-p_\chi\left(\tilde{J}(\xi)-1\right)}} \,. \tag{90}$$

This regularization is illustrated in Fig. 4 for different values of the regularization parameter $p_\chi \in (0, \infty)$. The black dashed line shows the discontinuous function. As the parameter p_χ

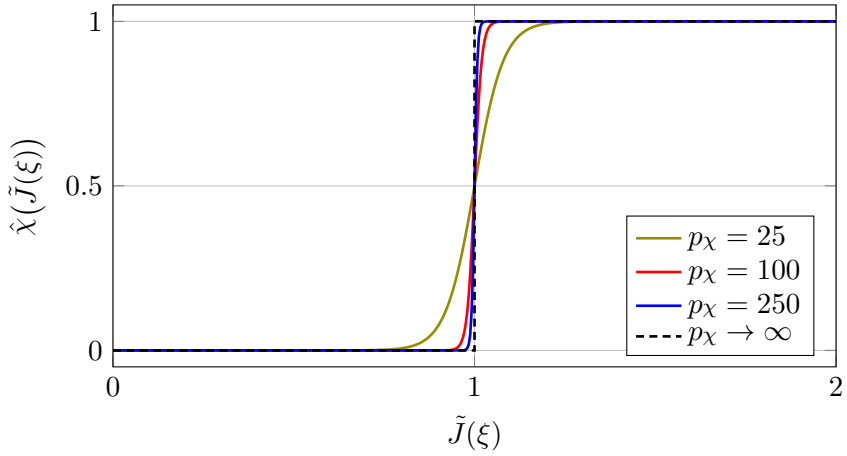

Figure 4: Smoothed jump function (cf. Eq. (90)) used to stabilize the Newton-Raphson solution scheme.

increases, the smoothed function $\hat{\chi}\big(\tilde{J}(\xi)\big)$ approximates the discontinuous function $\chi\big(\tilde{J}(\xi)\big)$ more precisely. By means of this smoothed function, the Newton-Raphson iteration does not alternate between different states and, in contrast to the active set strategy depicted above, no additional iteration is necessary. We note that an increase in the regularization parameter p_χ leads to a decrease in the average time steps computed by the adaptive time-stepping scheme in Sec. 5.5.2.

5.7 Dimensionless form

The preceding formulation is normalized by introduction of the reference length L_0, surface density ρ_0[6] and time T_0. The corresponding dimensionless quantities are

$$\boldsymbol{x}^\star = \frac{\boldsymbol{x}}{L_0} \,, \quad \rho^\star = \frac{\rho}{\rho_0} \,, \quad t^\star = \frac{t}{T_0} \,. \tag{91}$$

The normalization quantities for the in-plane material parameters K and G, the bending modulus c and the critical energy density $\mathcal{G}_\mathrm{c}$ then follow as

$$K^\star = \frac{K}{E_0} \,, \quad G^\star = \frac{G}{E_0} \,, \quad c^\star = \frac{c}{E_0\, L_0} \,, \quad \mathcal{G}_\mathrm{c}^\star = \frac{\mathcal{G}_\mathrm{c}}{E_0\, L_0} \,, \tag{92}$$

where $E_0 := \rho_0\, L_0^2\, T_0^{-2}$ has units [N/m]. The surface stress $\sigma^{\alpha\beta}$, the surface moment $M^{\alpha\beta}$, the surface tension γ, the elastic energy density Ψ and potential Π are then given by

$$\sigma_\star^{\alpha\beta} = \frac{\sigma^{\alpha\beta}}{E_0} \,, \quad M_\star^{\alpha\beta} = \frac{M^{\alpha\beta}}{E_0\, L_0} \,, \quad \gamma^\star = \frac{\gamma}{E_0} \,, \quad \Psi^\star = \frac{\Psi}{E_0} \,, \quad \Pi^\star = \frac{\Pi}{E_0\, L_0^2} \,. \tag{93}$$

[6]Note that ρ_0 is the surface density and has units [kg/m^2].

The temporal and spatial derivatives are (Zimmermann et al., 2019)

$$\frac{\partial \dots}{\partial t^\star} = T_0 \, \frac{\dots}{\partial t} \,, \quad \nabla_{\mathrm{S}}^\star = L_0 \, \nabla_{\mathrm{S}} \,, \quad \Delta_{\mathrm{S}}^\star = L_0^2 \, \Delta_{\mathrm{S}} \,. \tag{94}$$

In the following, the superscript $\star$ will be omitted for notational simplicity.

6 Numerical examples

This section shows several numerical examples of the proposed phase field formulation of brittle shells. The material parameters of the elastic energy density (cf. Sec. 4.2) are given via

$$K = \frac{E \, \nu}{(1+\nu)\,(1-2\nu)} \,, \qquad G = \frac{E}{2\,(1+\nu)} \,, \qquad c = 0.1 \, E_0 \, L_0 \,, \tag{95}$$

with stiffness E and Poisson's ratio ν. For all subsequently presented results, bi-quadratic LR NURBS are used and numerical integration on the bi-unit parent element is performed using Gaussian quadrature with 3×3 quadrature points. Numerical thickness integration is performed using four Gaussian quadrature points for all locations where the analytical integration formulae in Eqs. (47)–(48) do not apply. For the visualization, the surface tension

$$\gamma = \frac{1}{2} N_\alpha^\alpha \,, \tag{96}$$

is plotted, where N_α^α are the mixed components from the stress occurring in the equation of motion (18). All crack patterns are illustrated as follows: Red color resembles the fractured state ($\phi = 0$) and blue color indicates undamaged material ($\phi = 1$). In between these states, a transition based on the colors yellow-green-cyan is used.

Remark: The examples in this section exhibit stress waves. The present formulation does not consider any damping such that stress waves do not dissipate but continue to propagate and reflect. An artificial damping, e.g. based on energy absorbing boundary elements, could be employed. Alternatively, physical viscosity can be introduced in the system, similar as is done by Zimmermann et al. (2019). The challenge for the latter is to correctly split the viscous terms in analogy to the elastic split outlined in Sec. 4.2.1. Especially, the propagation of stress waves over elements of different size needs to be investigated further. The stress waves may be emitted from the crack, thus they might start propagating in regions of the highest resolved meshes. As they cross mesh interfaces (where elements of different sizes meet) it can happen that very fine waves are not represented on the coarse mesh. A damping strategy across these mesh interfaces could be employed to capture the stress waves more accurately.

6.1 2D shear test

The first example investigates crack evolution in a square two-dimensional membrane that is exposed to a shear load. The geometry including boundary and loading conditions is illustrated in Fig. 5. The mesh is initially constructed from 16×16 LR NURBS elements and the region next to the initial crack is refined by LR NURBS elements up to a refinement depth of $d = 5$, see Fig. 7. The material parameters are given in Tab. 1. The initial phase field distribution, which is induced by an initial history field, and the crack evolution are shown in Fig. 6. The crack evolves towards the bottom right corner on a curved path. The qualitative behavior resembles the results shown in the literature. For instance, in Borden et al. (2012) a quasi-static two-dimensional shear test has been investigated where the crack path has been locally refined *a*

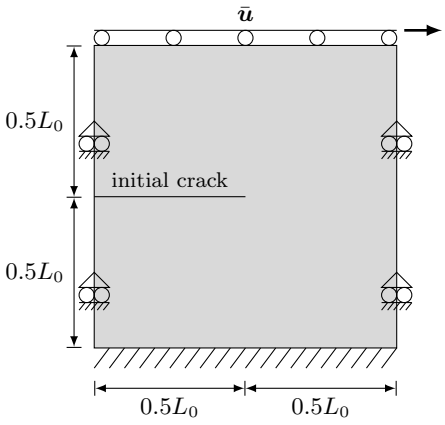

Figure 5: 2D shear test: Specimen geometry, boundary and loading conditions.

E $[E_0]$	ν $[-]$	$\Delta\bar{u}$ $[L_0]$	$\mathcal{G}_c$ $[E_0\,L_0]$	ℓ_0 $[L_0]$	T $[L_0]$
100	0.2	$2 \cdot 10^{-6}$	0.001	0.0025	0.0125

Table 1: 2D shear test: Material parameters and imposed load increment $\Delta\bar{u}$ per time step.

priori based on analysis-suitable T-splines.
Our results show that the split of the membrane energy from Sec. 4.2.1 works correctly since no branch is forming towards the specimen's top face. Based on the adaptive spatial refinement

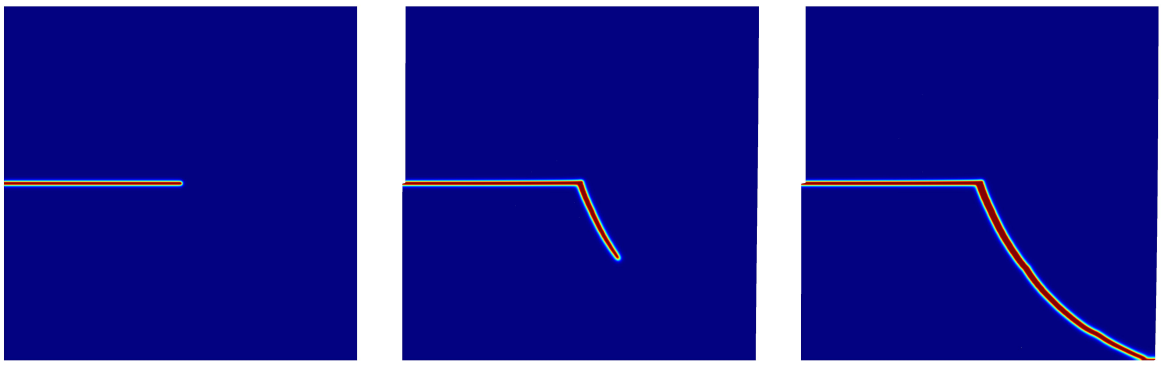

Figure 6: 2D shear test: Crack propagation at various time steps. The energy split for the membrane part of the elastic energy density leads to the qualitatively correct crack path.

strategy from Sec. 5.1.2, the LR mesh is refined as the crack evolves. The parametric domains of the LR meshes are illustrated in Fig. 7. Only the regions of damage are refined up to the prescribed refinement depth $d = 5$, while the periphery is kept coarse. Fig. 8 shows the time step sizes employed and the contributions to the total energy in the system. The latter have been computed from

$$\Pi_{\text{el}} = \int_{\mathcal{S}} \left(g(\phi)\Psi_{\text{el}}^{+} + \Psi_{\text{el}}^{-} \right) \mathrm{d}a\,, \quad \text{and} \quad \Pi_{\text{frac}} = \int_{\mathcal{S}} \Psi_{\text{frac}}\,\mathrm{d}a\,. \tag{97}$$

Fig. 8 shows that at the prescribed deformation $\bar{u} \in [0.001018, 0.004474]\,L_0$, the maximum time step size $\Delta t_{\max} = 0.1\,T_0$ is used since the crack is not evolving. Thus, the fracture energy stays constant during this time. Since the initial crack is modeled by means of an initial phase field,

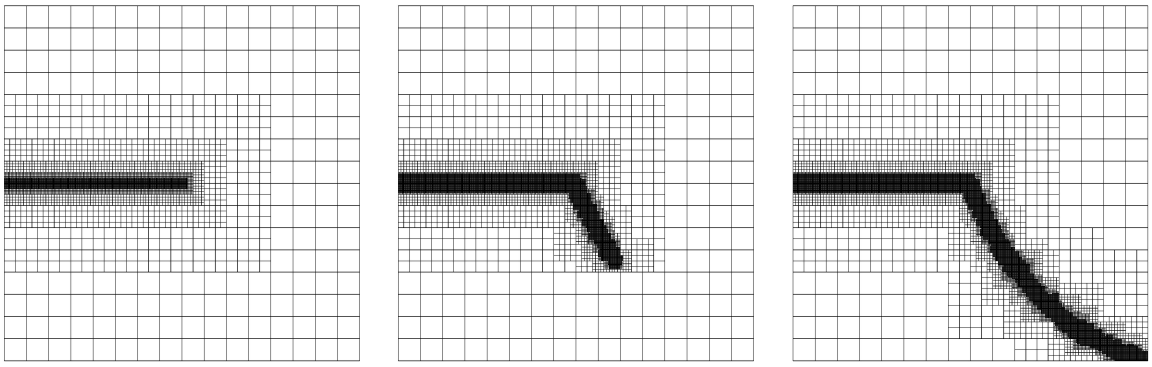

Figure 7: 2D shear test: Parametric domains of LR meshes at various time steps. Only damage regions are adaptively refined and a coarse mesh is kept in regions of no damage.

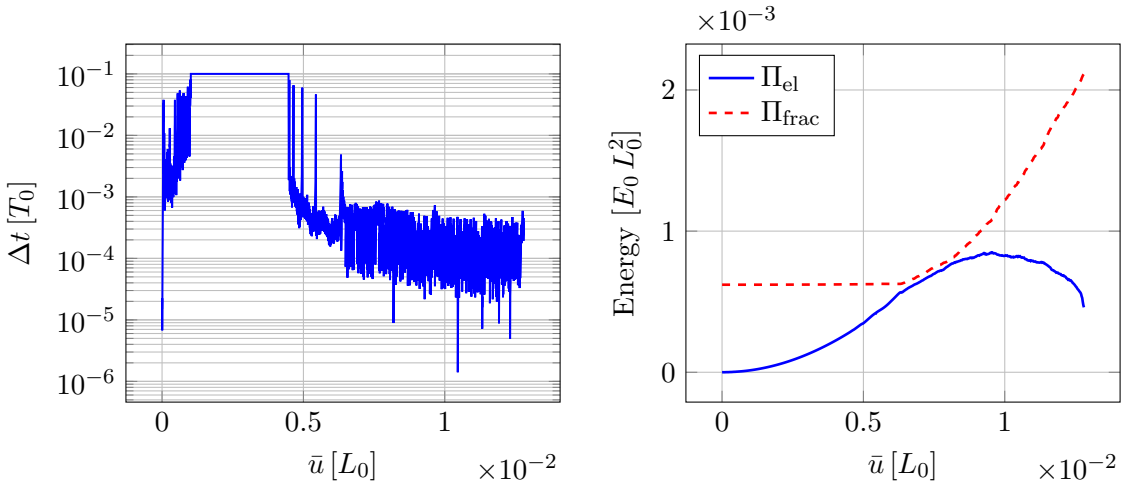

Figure 8: 2D shear test: Computed time step sizes on the left and elastic and fracture energy over the prescribed deformation $\bar{u}$ on the right. As the crack evolves, the fracture energy increases whereas the elastic energy decreases due to the degradation of the contribution Ψ_{el}^{+} (cf. Eq. (29)). The fracture energy is non-zero at $\bar{u} = 0\,L_0$ since the initial crack is modeled by means of an initial phase field.

the fracture energy is non-vanishing at $\bar{u} = 0\,L_0$. The elastic energy increases steadily due to the applied deformation. As the crack evolves at $\bar{u} > 0.006\,L_0$, the fracture energy increases, whereas the reduction of material stiffness leads to a decrease in elastic energy. Crack evolution takes place for $\bar{u} \in [0.006, 0.0128]\,L_0$.

6.2 Dynamic crack branching

We next consider a rectangular 2D membrane with an initial crack at the top. The problem setup is shown in Fig. 9a. A displacement of constant velocity is applied on the top face upwards and on the bottom face downwards. At each time step we impose the deformation increment $\Delta\bar{u} = \bar{v}\,\Delta t$ where the maximum time step size is set to $\Delta t_{\max} = 10^{-3}\,T_0$. The loading velocity is denoted $\bar{v}$. The material parameters are depicted in Tab. 2. The initial mesh is constructed from 64×32 LR NURBS elements and refined around the prescribed initial damage up to

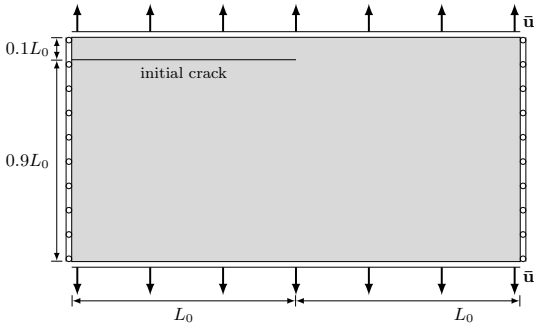

(a) Problem setup

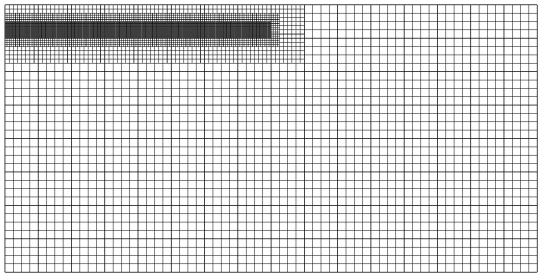

(b) Initial LR Mesh

Figure 9: Dynamic crack branching: (a) Specimen geometry, boundary and loading conditions and (b) initial LR mesh in which the region around the initial crack is refined up to a refinement depth of $d = 3$.

$E\ [E_0]$	$\nu\ [-]$	$\mathcal{G}_c\ [E_0\, L_0]$	$\ell_0\ [L_0]$	$T\ [L_0]$
100	0.3	0.001	0.0025	0.0125

Table 2: Dynamic crack branching: Material parameters.

a refinement depth $d = 3$, see Fig. 9b. The initial crack is not located on the mid-line so

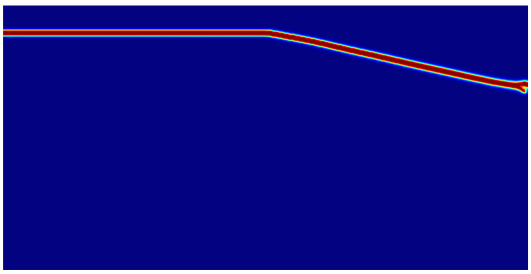

(a) $\bar{v} = 1.25 \cdot 10^{-3}\, L_0\, T_0^{-1}$

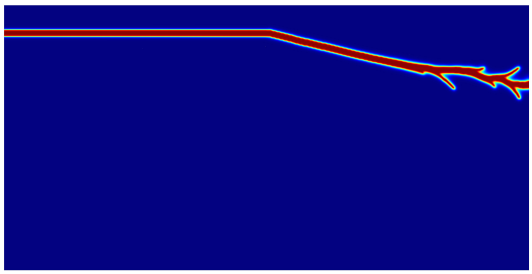

(b) $\bar{v} = 5 \cdot 10^{-3}\, L_0\, T_0^{-1}$

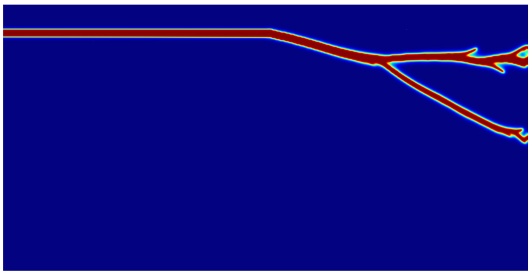

(c) $\bar{v} = 1 \cdot 10^{-2}\, L_0\, T_0^{-1}$

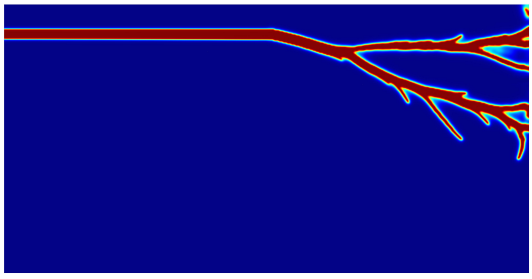

(d) $\bar{v} = 2 \cdot 10^{-2}\, L_0\, T_0^{-1}$

Figure 10: Dynamic crack branching: Crack evolution at the final state for different loading velocities $\bar{v}$. As the loading intensity is increased, crack branching occurs at an earlier time and closer to the left face of the membrane.

that the resulting asymmetric stress distribution leads to a deflection of the crack towards the bottom face, see Fig. 10. As the figure also shows, a higher loading velocity $\bar{v}$ leads to more complex fracture patterns with branching occurring sooner and more often. This makes their prediction *a priori* to the simulation very difficult. Fig. 11 shows the final LR meshes in the

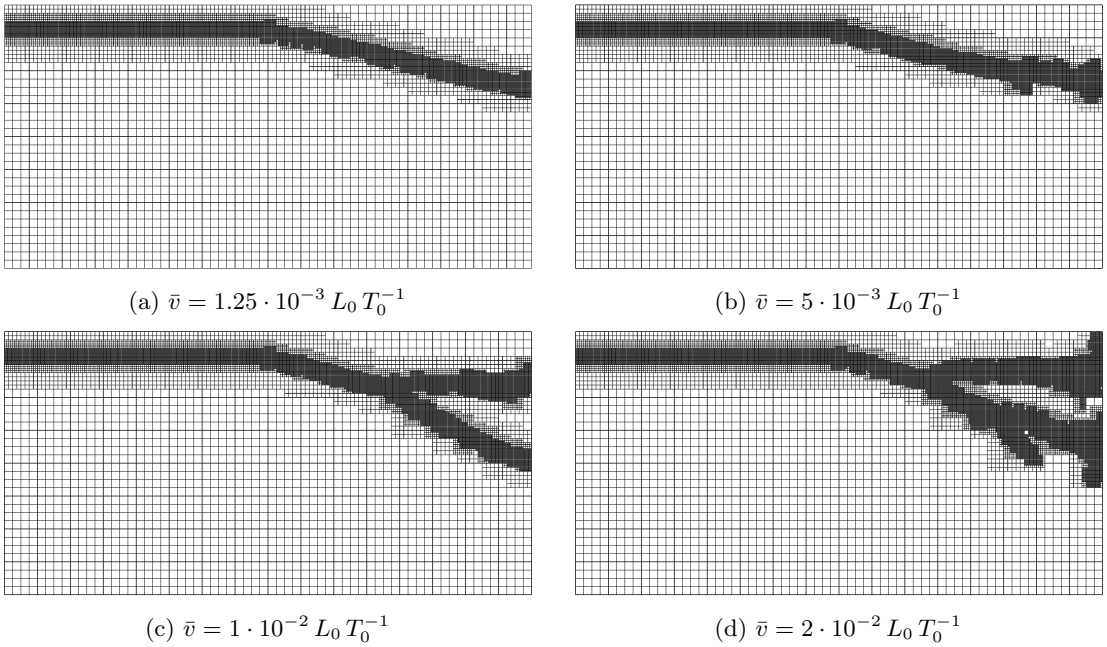

(a) $\bar{v} = 1.25 \cdot 10^{-3}\, L_0\, T_0^{-1}$ (b) $\bar{v} = 5 \cdot 10^{-3}\, L_0\, T_0^{-1}$

(c) $\bar{v} = 1 \cdot 10^{-2}\, L_0\, T_0^{-1}$ (d) $\bar{v} = 2 \cdot 10^{-2}\, L_0\, T_0^{-1}$

Figure 11: Dynamic crack branching: Final LR meshes as a function of the the loading velocity $\bar{v}$. The corresponding crack patterns are illustrated in Fig. 10.

undeformed configuration for the different crack patterns. There are large elements in regions of no fracture, whereas a highly resolved mesh is only obtained in the domain of fracture. Fig. 12 shows three snapshots of the crack evolution and the corresponding LR meshes for the loading intensity $\bar{v} = 2 \cdot 10^{-2}\, L_0\, T_0^{-1}$. The final states for these are shown in Figs. 10d and 11d. Only the periphery around the crack tip is refined, whereas no refinement is performed ahead of the crack tip. This adaptivity in space leads to an efficient prediction of fracture patterns.

6.3 Pressurized cylinder

In this example we study crack propagation on a curved surface. In the previous sections plane membranes without bending energy have been studied. The new problem setup is illustrated in Fig. 13. The corresponding parameters, including the imposed pressure $\bar{p}$ (cf. Eq. (82)), are listed in Tab. 3. We note that the pressure is not ramped up over time but imposed as an initial pressure shock in the interior of the cylinder. The maximum pressure is then kept constant over time. Fig. 14 illustrates the phase field evolution over time. Elements with $\phi < 0.001$ have

E $[E_0]$	ν $[-]$	$\bar{p}$ $[E_0\, L_0^{-1}]$	$\mathcal{G}_c$ $[E_0\, L_0]$	ℓ_0 $[L_0]$	T $[L_0]$
10	0.3	-0.1	0.00075	0.01	0.0125

Table 3: Pressurized cylinder: Material parameters and imposed pressure $\bar{p}$ (cf. Eq. (82)).

been removed for visualization. The crack propagates in axial direction until it branches into two cracks at each end. These branches propagate towards the cylinder ends. The radius at these ends is fixed, which serves as a stiffener of the structure in these regions. Thus, the cracks are deflected and continue propagating in radial direction. This shows the ability of our model to capture crack evolution, branching and deflection on curved surfaces. Additionally, it proves that it is able to handle large deformations: The last state shown in Fig. 14 at $t = 2.715125\, T_0$

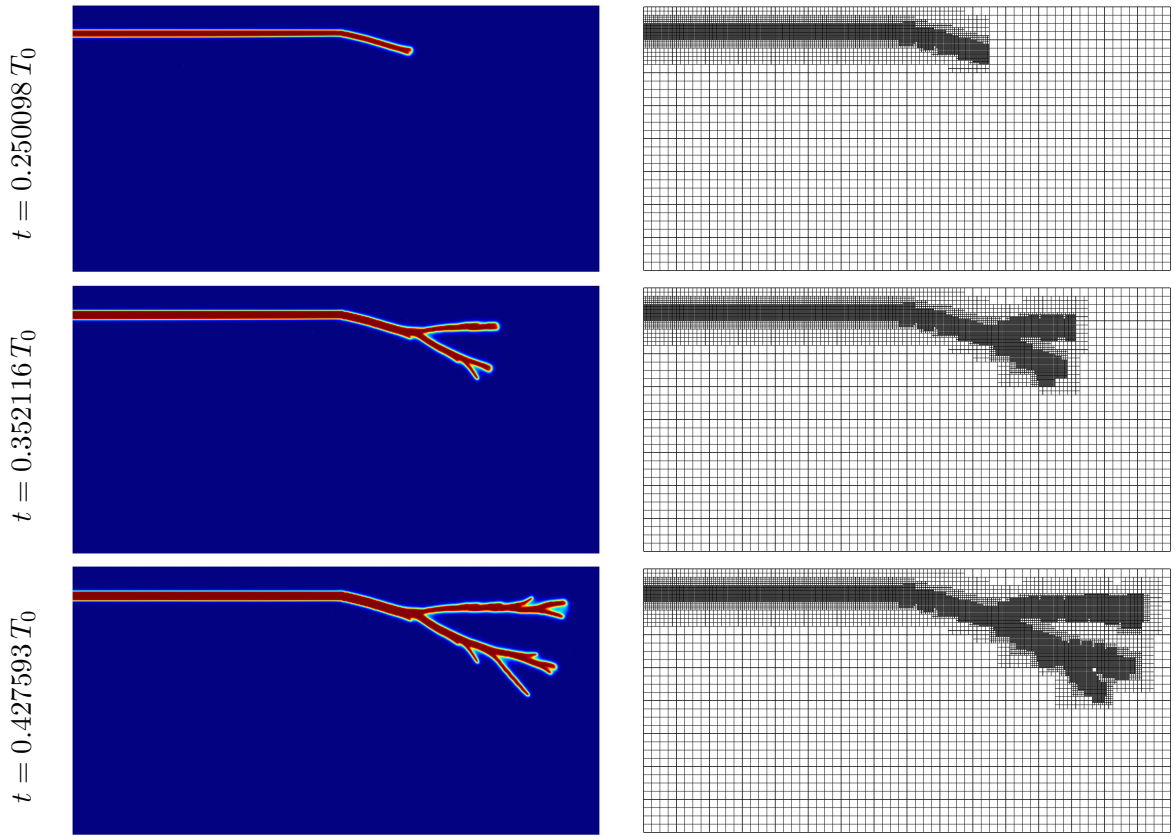

Figure 12: Dynamic crack branching: Evolution of the phase field on the left and corresponding LR meshes on the right. The loading intensity is $\bar{v} = 2 \cdot 10^{-2}\, L_0\, T_0^{-1}$. The final phase field and LR mesh are shown in Figs. 10d and 11d. See also the supplementary movie at https://doi.org/10.5446/42540.

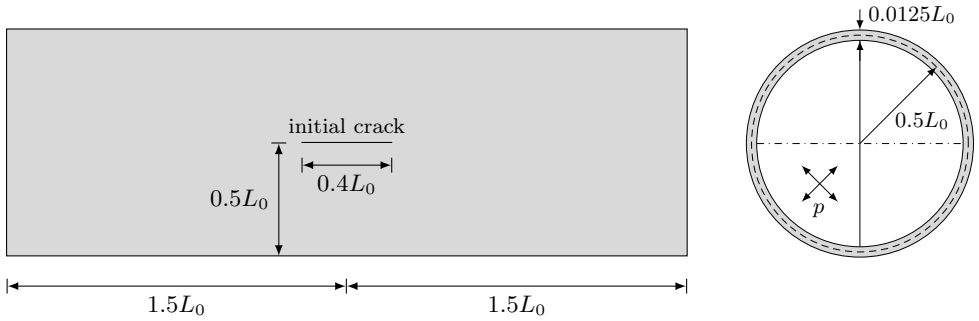

(a) Top view (b) Side view

Figure 13: Pressurized cylinder: Specimen geometry and loading conditions shown in (a) top view and (b) side view. The dashed line indicates the shell's mid plane. The shell is symmetric across the solid line in (b) which is used to reduce comutational effort. The movement of the two ends is only allowed in the axial direction and not in the radial direction.

includes maximum stretches of approximately 130.49%. In Fig. 15 the LR meshes for three different time steps are shown. In between the branches it is not refined as much as in the areas of fracture. The regions of no damage are kept coarse completely. As the crack is deflected in

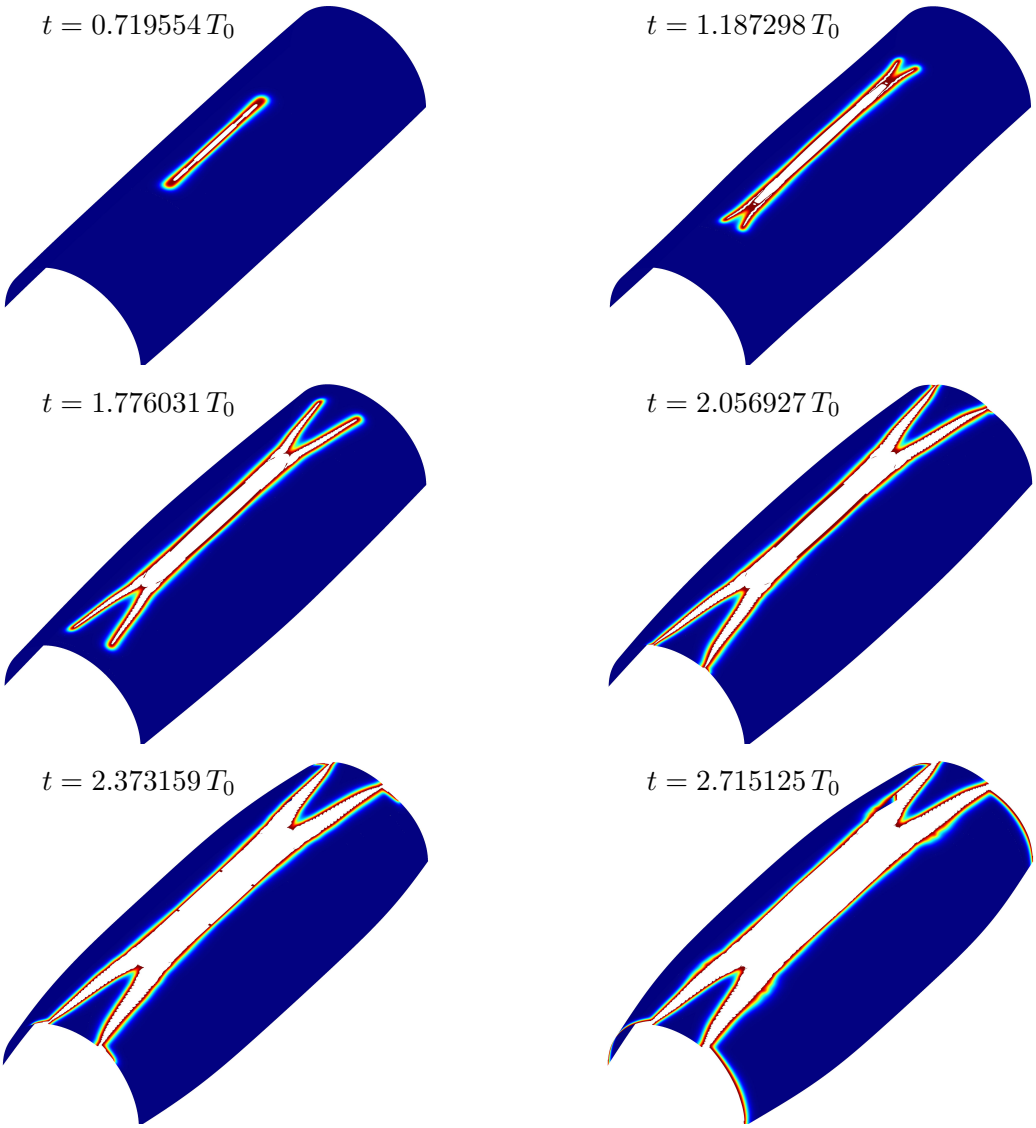

Figure 14: Pressurized cylinder: Crack pattern over time. The stretch reaches up to $\approx 130.49\%$ showing that the proposed formulation can model large deformations. Elements with $\phi < 0.001$ have been removed for visualization. See also the supplementary movie at https://doi.org/10.5446/42541.

radial direction, the cylinder ends are refined up to the prescribed refinement level $d = 3$. The initial mesh consists of $4,640$ elements and $4,572$ control points and the final mesh consists of $35,672$ elements and $34,756$ control points. A uniformly refined mesh would have $131,072$ elements and $128,777$ control points. The surface tension $\gamma(\boldsymbol{x}, t)$ (cf. Eq. (96)) is visualized in Fig. 16. Elements with $\phi < 0.001$ have been removed for visualization. Before the crack reaches the cylinder ends the maximum values are obtained at the crack tips. Small values are obtained behind the crack tip due to the emitted stress waves. The magnitude of the surface tension at the remaining areas is fluctuating due to reflection of stress waves and their following interaction. At the final state in Fig. 16, the largest stresses are obtained at the symmetry plane because the largest deformations occur there.

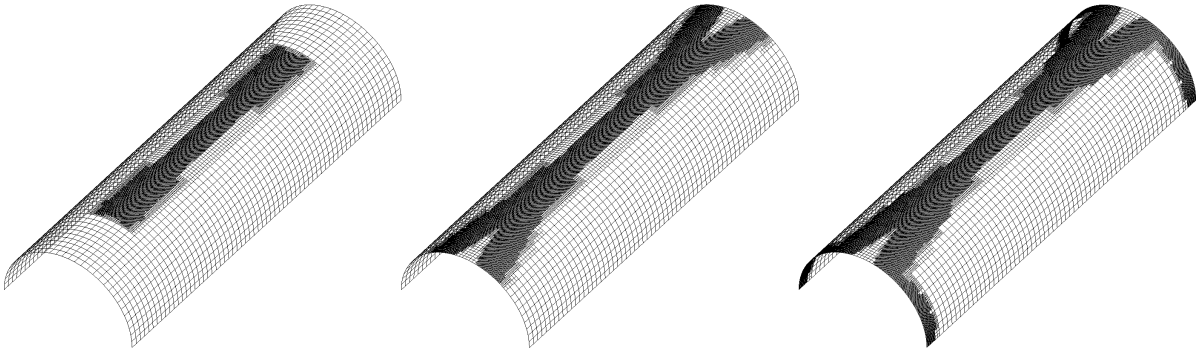

$t = 1.187298\,T_0$ $t = 2.056927\,T_0$ $t = 2.715125\,T_0$

Figure 15: Pressurized cylinder: LR meshes in the undeformed configuration during crack branching, before deflection and at the final state. See also the supplementary movie at https://doi.org/10.5446/42541.

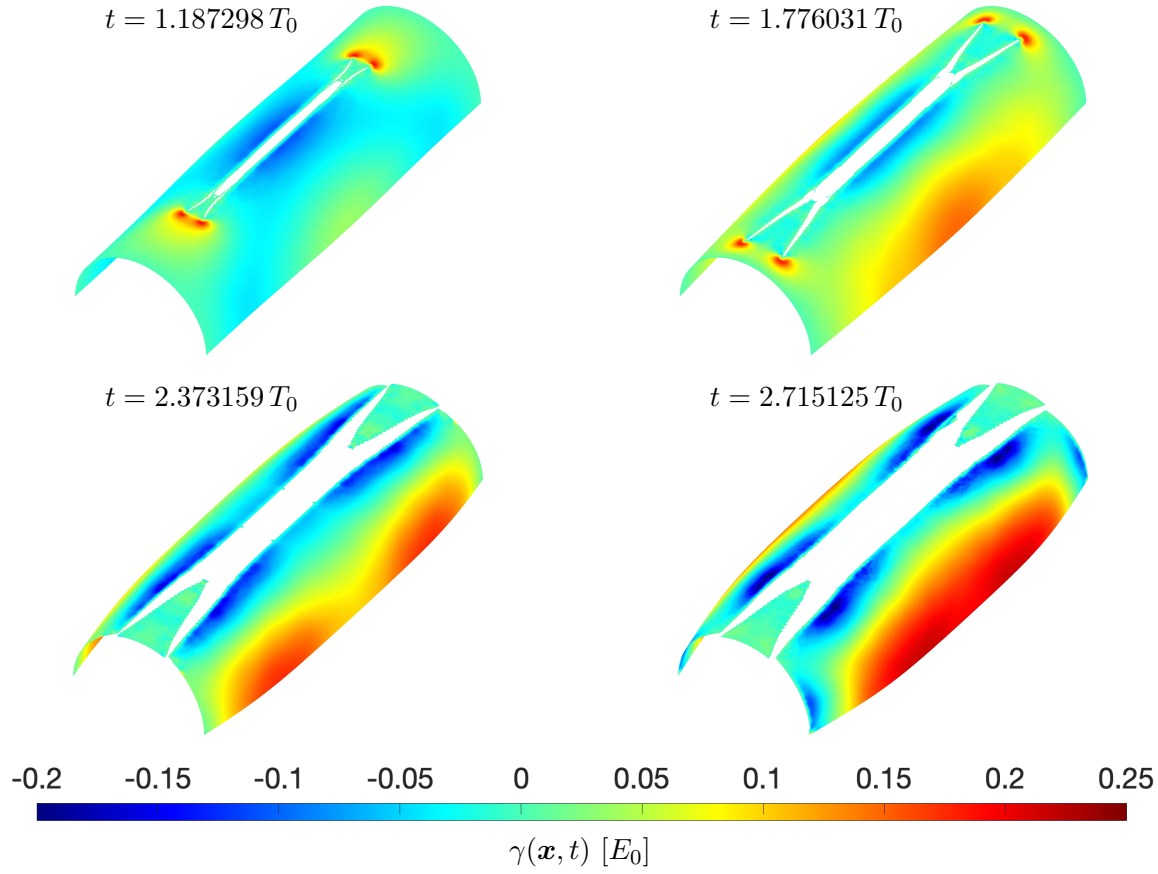

Figure 16: Pressurized cylinder: Surface tension γ (96) over time. Before the two branches reach the cylinder ends, the maximum values occur at the crack tip. Finally, the maximum values occur at the symmetry plane since the largest deformations occur there. Elements with $\phi < 0.001$ have been removed for visualization.

7 Conclusion

We have coupled a higher order phase field model for brittle fracture with a nonlinear thin shell formulation based on a curvilinear surface description. Given a split of the constitutive law into membrane and bending contributions, a split of the elastic energy density has been derived for these terms separately. No spectral decomposition of the strain tensor is required in our formulation. Instead, the surface stretch indicates if there is a contribution to crack evolution or not. We have adopted a thickness integration to capture the asymmetric distribution of volumetric compression and expansion around the mid-plane that occur due to bending. As a consequence, the phase field is constant throughout the thickness and is solely defined on the deforming two-dimensional manifold. A discretization over the thickness or multiple phase fields have thus been avoided by this formulation. The interface between fractured and intact material has been adaptively refined based on the current phase field value. Quadratic LR NURBS have been used for this in the numerical examples. Time discretization is based on a fully implicit generalized-α scheme with adaptive time-stepping, and a monolithic Newton-Raphson procedure is used to solve the discretized coupled system.

The examples presented in Sec. 6 include flat membranes and curved shells. For the flat cases, the results qualitatively resemble those presented in the literature. Studying crack propagation on a cylinder indicates the ability of our formulation to capture non-trivial fracture patterns on curved surfaces. It has been observed that the phase field value serves as a suitable indicator for local refinement since only areas along the crack paths are refined. The time step sizes are large if there is no crack evolution and are decreased as soon as the phase field starts evolving. Due to the adaptivity in space and time and the partially analytical thickness integration, the C^1-continuous solution is achieved within a computationally efficient framework.

Looking at the examples in Sec. 6, it does not seem to be necessary to keep a highly resolved mesh in regions of full damage ($\phi = 0$). An adaptive coarsening strategy could be employed, which coarsens the mesh at fully damaged regions. Thus, small elements would only be retained close to the crack tip. A coarsening method for LR NURBS is given in Zimmermann and Sauer (2017). Additionally, stress wave propagation and reflection should be further investigated. Stress wave decay could be modeled by introducing physical viscosity into the system. The corresponding viscous energy and stresses then need to be appropriately split, similar to the energy split outlined in Sec. 4.2.1. The reflection of stress waves at the boundaries could be damped by employing energy absorbing boundary layers. The same could be employed at the interfaces, where different element sizes meet to prevent reflection of stress waves at these LR mesh boundaries.

Acknowledgments

Thomas J.R. Hughes and Chad M. Landis were partially supported by the Office of Naval Research (Grant Nos. N00014-17-1-2119, N00014-13-1-0500, and N00014-17-1-2039). Kranthi K. Mandadapu acknowledges support from University of California Berkeley and from the National Institutes of Health Grant R01-GM110066. Roger A. Sauer acknowledges the support from a J. Tinsley Oden fellowship in 2016 and funding from the German Research Foundation (DFG) through project GSC 111. This work was partially funded by the Deutsche Forschungsgemeinschaft (DFG, German Research Foundation) 33849990/GRK2379 (IRTG Modern Inverse Problems). Simulations were performed with computing resources granted by RWTH Aachen University under project rwth0401.

Appendix

A Time integration scheme

The system in Eq. (87) with intermediate quantities and the quantities at time step $n+1$

$$\begin{aligned}
\mathbf{x}_{n+1} &= \mathbf{x}_n + \Delta t\,\dot{\mathbf{x}}_n + \big((0.5-\beta)\Delta t^2\big)\ddot{\mathbf{x}}_n + \beta\Delta t^2\ddot{\mathbf{x}}_{n+1}\,,\\
\dot{\mathbf{x}}_{n+1} &= \dot{\mathbf{x}}_n + \big((1-\gamma)\Delta t\big)\ddot{\mathbf{x}}_n + \gamma\Delta t\ddot{\mathbf{x}}_{n+1}\,,\\
\mathbf{x}_{n+\alpha_\mathrm{f}} &= \big(1-\alpha_\mathrm{f}\big)\mathbf{x}_n + \alpha_\mathrm{f}\mathbf{x}_{n+1}\,,\\
\dot{\mathbf{x}}_{n+\alpha_\mathrm{f}} &= \big(1-\alpha_\mathrm{f}\big)\dot{\mathbf{x}}_n + \alpha_\mathrm{f}\dot{\mathbf{x}}_{n+1}\,,\\
\ddot{\mathbf{x}}_{n+\alpha_\mathrm{m}} &= \big(1-\alpha_\mathrm{m}\big)\ddot{\mathbf{x}}_n + \alpha_\mathrm{m}\ddot{\mathbf{x}}_{n+1}\,,
\end{aligned} \tag{98}$$

has to be solved. Here, $\Delta t = t_{n+1} - t_n$ refers to the time step. Numerical dissipation is controlled by the parameters γ, β, α_f and α_m. They are expressed in terms of $\rho_\infty \in [0,1]$, which resembles an algorithmic parameter that corresponds to the spectral radius of the amplification matrix as $\Delta t \to \infty$ (see Chung and Hulbert (1993) for further details), i.e.

$$\begin{aligned}
\alpha_\mathrm{f} &= \frac{1}{1+\rho_\infty}\,, \quad \alpha_\mathrm{m} = \frac{2-\rho_\infty}{1+\rho_\infty}\,,\\
\gamma &= \frac{1}{2} + \alpha_\mathrm{m} - \alpha_\mathrm{f}\,, \quad \beta = \frac{1}{4}\left(1+\alpha_\mathrm{m}-\alpha_\mathrm{f}\right)^2.
\end{aligned} \tag{99}$$

We have found $\rho_\infty = 0.5$ to be a good choice and have used this in all computations. To solve the nonlinear system of equations in Eq. (87) using the Newton-Raphson procedure, it has to be linearized, i.e.

$$\begin{bmatrix} \mathbf{K}_\mathrm{x} & \mathbf{K}_\phi \\ \bar{\mathbf{K}}_\mathrm{x} & \bar{\mathbf{K}}_\phi \end{bmatrix} \begin{bmatrix} \Delta\mathbf{x}_{n+1} \\ \Delta\boldsymbol{\phi}_{n+1} \end{bmatrix} = -\begin{bmatrix} \mathbf{f}\left(\mathbf{x}_{n+\alpha_\mathrm{f}}, \ddot{\mathbf{x}}_{n+\alpha_\mathrm{m}}, \boldsymbol{\phi}_{n+1}\right) \\ \bar{\mathbf{f}}\left(\mathbf{x}_{n+\alpha_\mathrm{f}}, \boldsymbol{\phi}_{n+1}\right) \end{bmatrix}, \tag{100}$$

where the tangent matrix blocks are computed from

$$\begin{aligned}
\mathbf{K}_\mathrm{x} &= \frac{\partial \mathbf{f}}{\partial \mathbf{x}_{n+1}} = \alpha_\mathrm{f}\frac{\partial \mathbf{f}}{\partial \mathbf{x}_{n+\alpha_\mathrm{f}}} + \frac{\alpha_\mathrm{m}}{\beta\Delta t^2}\frac{\partial \mathbf{f}}{\partial \ddot{\mathbf{x}}_{n+\alpha_\mathrm{f}}}\,,\\
\mathbf{K}_\phi &= \frac{\partial \mathbf{f}}{\partial \boldsymbol{\phi}_{n+1}}\,,\\
\bar{\mathbf{K}}_\mathrm{x} &= \frac{\partial \bar{\mathbf{f}}}{\partial \mathbf{x}_{n+1}} = \alpha_\mathrm{f}\frac{\partial \bar{\mathbf{f}}}{\partial \mathbf{x}_{n+\alpha_\mathrm{f}}}\,,\\
\bar{\mathbf{K}}_\phi &= \frac{\partial \bar{\mathbf{f}}}{\partial \boldsymbol{\phi}_{n+1}}\,.
\end{aligned} \tag{101}$$

The required linearizations of the force vectors are shown in Appendix B. The initial guess for the Newton-Raphson iteration is set to

$$\begin{aligned}
\mathbf{x}^0_{n+1} &= \mathbf{x}_n + \Delta t\,\dot{\mathbf{x}}_n + \big((0.5-\beta)\Delta t^2\big)\ddot{\mathbf{x}}_n + \big(\beta\Delta t^2\big)\ddot{\mathbf{x}}^0_{n+1}\,,\\
\dot{\mathbf{x}}^0_{n+1} &= \dot{\mathbf{x}}_n\,,\\
\ddot{\mathbf{x}}^0_{n+1} &= \ddot{\mathbf{x}}_n\frac{\gamma-1}{\gamma}\,,\\
\boldsymbol{\phi}^0_{n+1} &= \boldsymbol{\phi}_n\,,
\end{aligned} \tag{102}$$

and then updated from iteration step $i \to i+1$ by

$$\begin{aligned}
\mathbf{x}_{n+1}^{i+1} &= \mathbf{x}_{n+1}^{i} + \Delta\mathbf{x}_{n+1}^{i+1} \,, \\
\dot{\mathbf{x}}_{n+1}^{i+1} &= \dot{\mathbf{x}}_{n+1}^{i} + \Delta\mathbf{x}_{n+1}^{i+1} \frac{1}{\gamma\,\Delta t} \,, \\
\ddot{\mathbf{x}}_{n+1}^{i+1} &= \ddot{\mathbf{x}}_{n+1}^{i} + \Delta\mathbf{x}_{n+1}^{i+1} \frac{1}{\beta\,\Delta t^2} \,, \\
\boldsymbol{\phi}_{n+1}^{i+1} &= \boldsymbol{\phi}_{n+1}^{i} + \Delta\boldsymbol{\phi}_{n+1}^{i+1} \,,
\end{aligned} \tag{103}$$

until convergence is achieved. At iteration i we check for the two convergence criteria

$$\max\left\{ \frac{\|\mathbf{f}_{n+1}^{i}\|}{\|\mathbf{f}_{n+1}^{0}\|}, \frac{\|\bar{\mathbf{f}}_{n+1}^{i}\|}{\|\bar{\mathbf{f}}_{n+1}^{0}\|} \right\} \leq \mathrm{tol}^{\mathrm{dyn}} \,, \tag{104}$$

with $\|...\|$ denoting the Euclidean norm and $\mathrm{tol}^{\mathrm{dyn}} = 10^{-4}$ and

$$\begin{bmatrix} \mathbf{f} \\ \bar{\mathbf{f}} \end{bmatrix} \cdot \begin{bmatrix} \Delta\mathbf{x} \\ \Delta\boldsymbol{\phi} \end{bmatrix} \leq \mathrm{tol}^{\mathrm{nrg}} \,, \tag{105}$$

with $\mathrm{tol}^{\mathrm{nrg}} = 10^{-25}$.

B Linearization

This section presents the respective elemental contributions for the tangent blocks in Eq. (101). The linearization of the mechanical force vector $\mathbf{f}^e := \mathbf{f}^e_{\mathrm{kin}} + \mathbf{f}^e_{\mathrm{int}} - \mathbf{f}^e_{\mathrm{ext}}$ of finite element Ω^e with respect to the respective nodal positions $\mathbf{x}_e$ can be found in the work of Duong et al. (2017). Since we model the pressure as a function of the phase field variable, we need to linearize the external force vector with respect to ϕ. This linearization of the pressure part $\mathbf{f}^e_{\mathrm{ext}p}$ of the external elemental force vector reads

$$\Delta_\phi\, \mathbf{f}^e_{\mathrm{ext}p} := \int_{\Omega^e} \mathbf{N}^{\mathrm{T}}\, \bar{p}\, \boldsymbol{n}^h\, \bar{\mathbf{N}}\, \mathrm{d}a\, \Delta\boldsymbol{\phi}_e \,. \tag{106}$$

For the linearization of the internal force vector the four material tangents

$$\begin{aligned}
c^{\alpha\beta\gamma\delta} &:= 2\frac{\partial \tau^{\alpha\beta}}{\partial a_{\gamma\delta}} \,, \qquad d^{\alpha\beta\gamma\delta} := \frac{\partial \tau^{\alpha\beta}}{\partial b_{\gamma\delta}} \,, \\
e^{\alpha\beta\gamma\delta} &:= 2\frac{\partial M_0^{\alpha\beta}}{\partial a_{\gamma\delta}} \,, \qquad f^{\alpha\beta\gamma\delta} := \frac{\partial M_0^{\alpha\beta}}{\partial b_{\gamma\delta}} \,,
\end{aligned} \tag{107}$$

have to be defined. Since we assume the constitutive in-plane response to be fully decoupled from the out-of-plane response, it follows that $d^{\alpha\beta\gamma\delta} = e^{\alpha\beta\gamma\delta} = 0$. According to Eqs. (49) and (50), the first tangent matrix can be computed based on the contributions

$$\begin{aligned}
\frac{\partial \tau^{\alpha\beta}_{\mathrm{dil}}}{\partial a_{\gamma\delta}} &= \frac{K}{2}\Big(J^2 a^{\alpha\beta} a^{\gamma\delta} + \left(J^2 - 1\right) a^{\alpha\beta\gamma\delta} \Big) \,, \\
\frac{\partial \tau^{\alpha\beta}_{\mathrm{dev}}}{\partial a_{\gamma\delta}} &= \frac{G}{2J}\left(\frac{I_1}{2} a^{\alpha\beta} a^{\gamma\delta} - I_1 a^{\alpha\beta\gamma\delta} - a^{\alpha\beta} A^{\gamma\delta} - A^{\alpha\beta} a^{\gamma\delta} \right) .
\end{aligned} \tag{108}$$

Based on Eqs. (52) and (53), the tangent matrix $f^{\alpha\beta\gamma\delta}$ can be computed with the contribution

$$\frac{\partial^2 \tilde{\Psi}_{\text{bend}}(\xi)}{\partial b_{\alpha\beta}\, \partial b_{\gamma\delta}} = \xi^2 \frac{12}{T^3}\, c\, A^{\alpha\gamma} A^{\beta\delta}\,. \tag{109}$$

Since we consider the fully linearized system in Eq. (100), we also need to linearize the mechanical force vector with respect to the phase field, i.e.

$$\Delta_\phi \mathbf{f}^e = \left[\mathbf{k}^e_{\sigma\phi} + \mathbf{k}^e_{M\phi}\right] \Delta\boldsymbol{\phi}_e\,, \tag{110}$$

with

$$\begin{aligned} \mathbf{k}^e_{\sigma\phi} &:= \int_{\Omega^e_0} g'(\phi)\, \tau^{\alpha\beta}_+\, \mathbf{N}^{\mathrm{T}}_{,\alpha}\, \boldsymbol{a}^h_\beta\, \bar{\mathbf{N}}\, \mathrm{d}A\,, \\ \mathbf{k}^e_{M\phi} &:= \int_{\Omega^e_0} g'(\phi)\, M^{\alpha\beta}_{0,+}\, \mathbf{N}^{\mathrm{T}}_{,\alpha\beta}\, \boldsymbol{n}^h\, \bar{\mathbf{N}}\, \mathrm{d}A\,, \end{aligned} \tag{111}$$

where $\tau^{\alpha\beta} := J\sigma^{\alpha\beta}$ and $M^{\alpha\beta}_0 := JM^{\alpha\beta}$ has been used to map the integrals to the element domain in the reference configuration. According to Eq. (86), the linearization of $\bar{\mathbf{f}}^e$ with respect to the respective nodal positions $\mathbf{x}_e$ yields

$$\Delta_{\mathrm{x}} \bar{\mathbf{f}}^e_{\text{el}} := \int_{\Omega^e_0} \bar{\mathbf{N}}^{\mathrm{T}} \frac{2\ell_0}{\mathcal{G}_{\mathrm{c}}} g'(\phi)\, \Delta_{\mathrm{x}}\mathcal{H}\, \mathrm{d}A\, \Delta\mathbf{x}_{\mathrm{e}}\,, \tag{112}$$

with

$$\Delta_{\mathrm{x}}\mathcal{H} := \Delta_{\mathrm{x}} \max_{\tau\in[0,t]} \Psi^+_{\text{el}}(\boldsymbol{x},\tau)\,, \tag{113}$$

and

$$\Delta_{\mathrm{x}}\Psi^+_{\text{el}} := \tau^{\alpha\beta}_{\text{el},+}\, \boldsymbol{a}_\alpha \cdot \mathbf{N}_{,\beta} + M^{\alpha\beta}_{0,+}\, \boldsymbol{n}\cdot\mathbf{N}_{,\alpha\beta}\,. \tag{114}$$

The linearization of $\bar{\mathbf{f}}^e_{\text{int}}$ with respect to the phase field variables of Ω^e reads

$$\Delta_\phi \bar{\mathbf{f}}^e_{\text{int}} := \left[\bar{\mathbf{k}}^e_0 + \bar{\mathbf{k}}^e_{\text{el}}\right] \Delta\boldsymbol{\phi}_{\mathrm{e}}\,, \tag{115}$$

with

$$\bar{\mathbf{k}}^e_{\text{el}} := \int_{\Omega^e_0} \bar{\mathbf{N}}^{\mathrm{T}} \left(\frac{2\ell_0}{\mathcal{G}_{\mathrm{c}}} g''(\phi)\mathcal{H}\right) \bar{\mathbf{N}}\, \mathrm{d}A\,. \tag{116}$$

The matrices $\bar{\mathbf{k}}^e_0$ and $\bar{\mathbf{k}}^e_{\text{el}}$ both contribute to the tangent block $\bar{\mathbf{K}}_\phi$ in Eq. (100).

References

Ambati, M. and De Lorenzis, L. (2016). Phase-field modeling of brittle and ductile fracture in shells with isogeometric NURBS-based solid-shell elements. *Computer Methods in Applied Mechanics and Engineering*, **312**:351—373.

Ambati, M., Gerasimov, T., and De Lorenzis, L. (2015). A review on phase-field models of brittle fracture and a new fast hybrid formulation. *Computational Mechanics*, **55**(2):383–405.

Ambati, M., Kruse, R., and De Lorenzis, L. (2016). A phase-field model for ductile fracture at finite strains and its experimental verification. *Computational Mechanics*, **57**(1):149–167.

Amiri, F., Milln, D., Shen, Y., Rabczuk, T., and Arroyo, M. (2014). Phase-field modeling of fracture in linear thin shells. *Theoretical and Applied Fracture Mechanics*, **69**:102–109.

Amor, H., Marigo, J.-J., and Maurini, C. (2009). Regularized formulation of the variational brittle fracture with unilateral contact: Numerical experiments. *Journal of the Mechanics and Physics of Solids*, **57**(8):1209–1229.

Areias, P., Rabczuk, T., and Msekh, M. (2016). Phase-field analysis of finite-strain plates and shells including element subdivision. *Computer Methods in Applied Mechanics and Engineering*, **312**:322–350.

Badnava, H., Msekh, M. A., Etemadi, E., and Rabczuk, T. (2018). An h-adaptive thermo-mechanical phase field model for fracture. *Finite Elements in Analysis and Design*, **138**:31–47.

Benson, D. J., Hartmann, S., Bazilevs, Y., Hsu, M.-C., and Hughes, T. J. R. (2013). Blended isogeometric shells. *Computer Methods in Applied Mechanics and Engineering*, **255**:133–146.

Borden, M. J., Hughes, T. J. R., Landis, C. M., Anvari, A., and Lee, I. J. (2016). A phase-field formulation for fracture in ductile materials: Finite deformation balance law derivation, plastic degradation, and stress triaxiality effects. *Computer Methods in Applied Mechanics and Engineering*, **312**:130–166.

Borden, M. J., Hughes, T. J. R., Landis, C. M., and Verhoosel, C. V. (2014). A higher-order phase-field model for brittle fracture: Formulation and analysis within the isogeometric analysis framework. *Computer Methods in Applied Mechanics and Engineering*, **273**:100–118.

Borden, M. J., Verhoosel, C. V., Scott, M. A., Hughes, T. J. R., and Landis, C. M. (2012). A phase-field description of dynamic brittle fracture. *Computer Methods in Applied Mechanics and Engineering*, **217–220**:77–95.

Bourdin, B., Francfort, G., and Marigo, J.-J. (2000). Numerical experiments in revisited brittle fracture. *Journal of the Mechanics and Physics of Solids*, **48**(4):797–826.

Bourdin, B., Larsen, C. J., and Richardson, C. L. (2011). A time-discrete model for dynamic fracture based on crack regularization. *International Journal of Fracture*, **168**(2):133–143.

Chung, J. and Hulbert, G. M. (1993). A time integration algorithm for structural dynamics with improved numerical dissipation: The generalized-alpha method. *Journal of Applied Mechanics*, **60**(2):371–375.

Ciarlet, P. G. (1993). *Mathematical Elasticity: Three Dimensional Elasticity*. North-Holland.

Dokken, T., Lyche, T., and Pettersen, K. F. (2013). Polynomial splines over locally refined box-partitions. *Computer Aided Geometric Design*, **30**(3):331–356.

Duong, T. X., Roohbakhshan, F., and Sauer, R. A. (2017). A new rotation-free isogeometric thin shell formulation and a corresponding continuity constraint for patch boundaries. *Computer Methods in Applied Mechanics and Engineering*, **316**:43–83.

Echter, R., Oesterle, B., and Bischoff, M. (2013). A hierarchic family of isogeometric shell finite elements. *Computer Methods in Applied Mechanics and Engineering*, **254**:170–180.

Forsey, D. R. and Bartels, R. H. (1988). Hierarchical B-spline refinement. *SIGGRAPH Comput. Graph.*, **22**(4):205–212.

Francfort, G. and Marigo, J.-J. (1998). Revisiting brittle fracture as an energy minimization problem. *Journal of the Mechanics and Physics of Solids*, **46**(8):1319–1342.

Gerasimov, T. and De Lorenzis, L. (2016). A line search assisted monolithic approach for phase-field computing of brittle fracture. *Computer Methods in Applied Mechanics and Engineering*, **312**:276 – 303.

Gerasimov, T. and De Lorenzis, L. (2018). On penalization in variational phase-field models of brittle fracture. *https://arxiv.org*, 1811.05334.

Gerasimov, T., Noii, N., Allix, O., and De Lorenzis, L. (2018). A non-intrusive global/local approach applied to phase-field modeling of brittle fracture. *Advanced Modeling and Simulation in Engineering Sciences*, **5**.

Gomez, H., Reali, A., and Sangalli, G. (2014). Accurate, efficient, and (iso)geometrically flexible collocation methods for phase-field models. *Journal of Computational Physics*, **262**:153–171.

Griffith, A. (1921). VI. The phenomena of rupture and flow in solids. *Philosophical Transactions of the Royal Society of London A: Mathematical, Physical and Engineering Sciences*, **221**(582-593):163–198.

Hesch, C., Franke, M., Dittmann, M., and Temizer, İ. (2016a). Hierarchical NURBS and a higher-order phase-field approach to fracture for finite-deformation contact problems. *Computer Methods in Applied Mechanics and Engineering*, **301**:242 – 258.

Hesch, C., Schu, S., Dittmann, M., Franke, M., and Weinberg, K. (2016b). Isogeometric analysis and hierarchical refinement for higher-order phase-field models. *Computer Methods in Applied Mechanics and Engineering*, **303**:185–207.

Hofacker, M. and Miehe, C. (2012). A phase field model of dynamic fracture: Robust field updates for the analysis of complex crack patterns. *International Journal for Numerical Methods in Engineering*, **93**(3):276–301.

Hughes, T. J. R., Cottrell, J., and Bazilevs, Y. (2005). Isogeometric Analysis: CAD, finite elements, NURBS, exact geometry and mesh refinement. *Computer Methods in Applied Mechanics and Engineering*, **194**(39-41):4135–4195.

Johannessen, K. A., Kvamsdal, T., and Dokken, T. (2014). Isogeometric analysis using LR B-splines. *Computer Methods in Applied Mechanics and Engineering*, **269**:471–514.

Karma, A., Kessler, D., and Levine, H. (2001). Phase-field model of mode III dynamic fracture. *Physical Review Letters*, **75**.

Kästner, M., Hennig, P., Linse, T., and Ulbricht, V. (2016). Phase-field modelling of damage and fracture — convergence and local mesh refinement. In Naumenko, K. and Aßmus, M., editors, *Advanced Methods of Continuum Mechanics for Materials and Structures*, pages 307–324. Springer Singapore, Singapore.

Kiendl, J., Ambati, M., De Lorenzis, L., Gomez, H., and Reali, A. (2016). Phase-field description of brittle fracture in plates and shells. *Computer Methods in Applied Mechanics and Engineering*, **312**:374–394.

Kiendl, J., Hsu, M.-C., Wu, M. C. H., and Reali, A. (2015). Isogeometric Kirchhoff-Love shell formulations for general hyperelastic materials. *Computer Methods in Applied Mechanics and Engineering*, **291**:280–303.

Krueger, R. (2002). Virtual crack closure technique: History, approach, and applications. *Applied Mechanics Reviews*, **57**.

Kuhn, C. and Müller, R. (2010). A continuum phase field model for fracture. *Engineering Fracture Mechanics*, **77**(18):3625–3634.

Kuhn, C., Schlüter, A., and Müller, R. (2015). On degradation functions in phase field fracture models. *Computational Materials Science*, **108**:374–384. Selected Articles from Phase-field Method 2014 International Seminar.

Larsen, C., Ortner, C., and Süli, E. (2010). Existence of solutions to a regularized model of dynamic fracture. *Mathematical Models and Methods in Applied Sciences*, **20**:1021–1048.

Larsen, C. J. (2010). Models for dynamic fracture based on Griffith's criterion. In Hackl, K., editor, *IUTAM Symposium on Variational Concepts with Applications to the Mechanics of Materials*, pages 131–140, Dordrecht. Springer Netherlands.

Miehe, C., Hofacker, M., and Welschinger, F. (2010a). A phase field model for rate-independent crack propagation: Robust algorithmic implementation based on operator splits. *Computer Methods in Applied Mechanics and Engineering*, **199**(45):2765–2778.

Miehe, C., Welschinger, F., and Hofacker, M. (2010b). Thermodynamically consistent phase-field models of fracture: Variational principles and multi-field FE implementations. *International Journal for Numerical Methods in Engineering*, **83**:1273–1311.

Moës, N., Dolbow, J., and Belytschko, T. (1999). A finite element method for crack growth without remeshing. *International Journal for Numerical Methods in Engineering*, **46**:131–150.

Nagaraja, S., Elhaddad, M., Ambati, M., Kollmannsberger, S., De Lorenzis, L., and Rank, E. (2018). Phase-field modeling of brittle fracture with multi-level hp-FEM and the finite cell method. *Computational Mechanics*.

Naghdi, P. M. (1973). The theory of shells and plates. In Truesdell, C., editor, *Linear Theories of Elasticity and Thermoelasticity: Linear and Nonlinear Theories of Rods, Plates, and Shells*, pages 425–640, Berlin, Heidelberg. Springer.

Parvizian, J., Düster, A., and Rank, E. (2007). Finite cell method. *Computational Mechanics*, **41**(1):121–133.

Reali, A. and Hughes, T. J. R. (2015). *An Introduction to Isogeometric Collocation Methods*, pages 173–204. Springer Vienna, Vienna.

Reinoso, J., Paggi, M., and Linder, C. (2017). Phase field modeling of brittle fracture for enhanced assumed strain shells at large deformations: formulation and finite element implementation. *Computational Mechanics*, **59**(6):981–1001.

Remmers, J., Borst, R., and Needleman, A. (2003). A cohesive segments method for the simulation of crack growth. *Compuational Mechanics*, **31**:69–77.

Sahu, A., Sauer, R. A., and Mandadapu, K. K. (2017). Irreversible thermodynamics of curved lipid membranes. *Physical Review E*, **96**:042409.

Sargado, J. M., Keilegavlen, E., Berre, I., and Nordbotten, J. M. (2018). High-accuracy phase-field models for brittle fracture based on a new family of degradation functions. *Journal of the Mechanics and Physics of Solids*, **111**:458–489.

Sauer, R. A. (2018). On the computational modeling of lipid bilayers using thin-shell theory. In Steigmann, D. J., editor, *The Role of Mechanics in the Study of Lipid Bilayers*, pages 221–286. Springer International Publishing, Cham.

Sauer, R. A. and Duong, T. X. (2017). On the theoretical foundations of thin solid and liquid shells. *Mathematics and Mechanics of Solids*, **22**(3):343–371.

Sauer, R. A., Duong, T. X., and Corbett, C. J. (2014). A computational formulation for constrained solid and liquid membranes considering isogeometric finite elements. *Comput. Methods Appl. Mech. Engrg.*, **271**:48–68.

Sauer, R. A., Duong, T. X., Mandadapu, K. K., and Steigmann, D. J. (2017). A stabilized finite element formulation for liquid shells and its application to lipid bilayers. *Journal of Computational Physics*, **330**:436–466.

Schillinger, D., Borden, M. J., and Stolarski, H. K. (2015). Isogeometric collocation for phase-field fracture models. *Computer Methods in Applied Mechanics and Engineering*, **284**:583–610.

Schlüter, A., Willenbücher, A., Kuhn, C., and Müller, R. (2014). Phase field approximation of dynamic brittle fracture. *Computational Mechanics*, **54**(5):1141–1161.

Sederberg, T. W., Zheng, J., Bakenov, A., and Nasri, A. (2003). T-splines and T-NURCCs. *ACM Transactions on Graphics*, **22**(3):477–484.

Steigmann, D. J. (1999). Fluid films with curvature elasticity. *Archive for Rational Mechanics and Analysis*, **150**:127–152.

Ulmer, H., Hofacker, M., and Miehe, C. (2012). Phase field modeling of fracture in plates and shells. *PAMM*, **12**(1):171–172.

Zhou, S. and Zhuang, X. (2018). Adaptive phase field simulation of quasi-static crack propagation in rocks. *Underground Space*, **3**(3):190–205.

Zimmermann, C. and Sauer, R. A. (2017). Adaptive local surface refinement based on LR NURBS and its application to contact. *Computational Mechanics*, **60**:1011–1031.

Zimmermann, C., Toshniwal, D., Landis, C. M., Hughes, T. J. R., Mandadapu, K. K., and Sauer, R. A. (2019). An isogeometric finite element formulation for phase transitions on deforming surfaces. *Computer Methods in Applied Mechanics and Engineering*, **351**:441–477.